ELSEVIER

Infrared metasurface-enabled compact polarization nanodevices

Guangtao Cao [1,2,4,†], He-Xiu Xu [2,7,†], Lei-Ming Zhou [2,5], Yan Deng [2], Yixuan Zeng [2], Shaohua Dong [2], Qing Zhang [2], Yangjun Li [6], Hui Yang [3,4,*], Qinghai Song [8], Xinke Liu [1,*], Ying Li [9,10], Cheng-Wei Qiu [2,*]

[1] College of Materials Science and Engineering, Shenzhen University-Hanshan Normal University Post Doctoral Workstation, Shenzhen University, Shenzhen 518060, China
[2] Department of Electrical and Computer Engineering, National University of Singapore Kent Ridge, Singapore 117583, Singapore
[3] Nanophotonics Research Center, Shenzhen Key Laboratory of Micro-scale Optical Information Technology, Institute of Microscale Optoelectronics, Shenzhen University, Shenzhen 518060, Guangdong, China
[4] School of Physics and Electronic Sciences, Changsha University of Science and Technology, Changsha 410004, China
[5] Department of Optical Science and Engineering, Hefei University of Technology, Hefei, Anhui 230009, China
[6] State Key Laboratory of Infrared Physics, Shanghai Institute of Technical Physics, Chinese Academy of Sciences, 500 Yu Tian Road, Shanghai, 200083, China
[7] Air and Missile Defense College, Air Force Engineering University, Xi'an 710051, China
[8] State Key Laboratory on Tunable Laser Technology, Ministry of Industry and Information Technology Key Laboratory of Micro-Nano Optoelectronic Information System, Shenzhen Graduate School, Harbin Institute of Technology, Shenzhen 518055, China
[9] Interdisciplinary Center for Quantum Information, State Key Laboratory of Modern Optical Instrumentation, ZJU-Hangzhou Global Scientific and Technological Innovation Center, Zhejiang University, Hangzhou 310027, China
[10] International Joint Innovation Center, Key Lab. of Advanced Micro/Nano Electronic Devices & Smart Systems of Zhejiang, The Electromagnetics Academy of Zhejiang University, Zhejiang University, Haining 314400, China

Infrared metasurface, especially that having a working range covering wavelengths from 0.75 to 25 μm, has been exploited as a revolutionary tool to manipulate the properties of electromagnetic waves owing to its potential applications in military and civilian fields. It owns the capacity to steer electromagnetic waves within subwavelength scale, with full degrees of freedom such as phase, amplitude and polarization, allowing the development of a number of planar meta-devices including the metalens, hologram, wave-plate and polarimeter. In particular, polarization, which determines the interaction of electromagnetic waves with matter, is important in almost every area of science. However, conventional materials for infrared polarization control inevitably introduce extra optical components and bulky configurations, hindering future miniaturization and integration. Moreover, compared with their short wavelength counterparts, polarization nanodevices in the infrared band and especially those in the long-wavelength infrared region have been far less explored due to the loss of material and immature fabrication techniques. Here, we review recent progress in the development of infrared metasurfaces in terms of generating, manipulating and detecting the polarization on standard and higher-order Poincaré spheres. The principles, typical strategies and emerging applications of these processes are introduced. We also discuss the challenges and outlook of future developments in this emerging field.

* Corresponding authors.
E-mail addresses: Yang, H. (yangh1023@126.com), Liu, X. (xkliu@szu.edu.cn), Qiu, C.-W. (chengwei.qiu@nus.edu.sg).
† These authors contributed equally to this work.

 https://doi.org/10.1016/j.mattod.2021.06.014

Keywords: Metasurface; Infrared; Polarization; Poincaré sphere

Introduction

Metasurfaces, the two-dimensional counterparts of metamaterials, have been regarded as a major advance in the field of nano-optics [1–3]. The abilities of metasurfaces to locally modify the amplitude, phase and polarization of light have radically changed the way to engineer the light-matter interactions. Metasurfaces are typically composed of artificially designed meta-atoms and hence own adjustable electromagnetic parameters, unlocking exceptional functionalities which otherwise are not feasible for conventional materials. Additionally, having strong wavefront-shaping capabilities and subwavelength thickness, metasurfaces promise to be excellent platforms in the design of planar and integrated optical devices [4,5]. Up to now, various metasurfaces have been implemented to realize all kinds of phenomenon and meta-devices, such as the spin-Hall effect [6–11], metalenses [12–19], polarization modulators [20–32], meta-holograms [33–42], structured light generators [43–48], and near-field configurations [49–61], covering various wavelength bands (including ultraviolet, visible, infrared (IR), terahertz, microwave and millimeter wave regions).

The IR spectral region (spanning wavelengths of 0.75 to 300 μm) is of vital importance to numerous military and civilian applications, such as thermal imaging, remote sensing and wireless communication [62,63]. For example, the mid-IR region covering 8–20 μm is often referred to as the "fingerprint region" since many molecules have uniquely identifiable absorption within it. In particular, the sensing wavelengths of a variety of gases, including CO_2 (2.65 μm, 4.2–4.3 μm), CH_4 (3.2–3.45 μm), and CO (~4.5 μm), are located in this wavelength region. Moreover, the IR atmospheric windows of 3–5 μm and 8–11 μm facilitate numerous applications, such as thermal imaging and free-space wireless communication. Nowadays, the rapid development of metasurfaces has enabled a number of planar and compact functional nanodevices in the IR range. However, most of the proposed meta-devices operate in the near-IR band, and optical engineering in the remaining IR bands suffers from technical challenges because most traditional optical materials (e.g. silicate glasses and optical polymers) are opaque at wavelengths beyond 3 μm [64]. Some specific materials such as halides and chalcogenides, have good performance in the mid-IR and far-IR bands, however, suffers from difficult processing technologies [62,65]. Apart from the challenges related to the IR materials, another issue to overcome is the expense of experiments. The experimental instruments used in mid-IR wavebands, such as cameras and quantum cascade lasers, are much more expensive than those operating in the near-IR and visible wavebands. Metasurface-enabled nanodevices used at various wavelengths usually have similar design strategies, and researchers thus tend to choose the cheaper/easier options in the near-IR and visible wavebands to provide a proof of concept. Consequently, in contrast to the long and broad development of visible and near-IR metasurfaces, mid-IR and far-IR metasurfaces are still in early development stage. Meanwhile, the miniaturization of planar meta-devices used at short wavelengths will be constrained by available fabrication techniques, while miniaturization in the IR region is more promising.

Over the last decades, metasurfaces in the IR range have been shown to be superior in terms of manipulating electromagnetic waves with full degrees of freedom; e.g., the manipulation of [66–68], frequency [69–73], phase [12,17,74,75], polarization [21,22] and even multiple parameters of output light can be manipulated simultaneously [68,76–78]. Among them, IR metasurface-enabled polarization control on both the standard Poincaré sphere (PS) and higher-order Poincaré spheres (HOPSs) has attracted great attentions (as shown in Fig. 1). Polarization, one of the intrinsic properties of an electromagnetic wave, characterizes the vectorial nature of an oscillating electric field. It also determines how an electromagnetic wave interacts with matter, forming the basis of a variety of optical technologies in the fields of optical sensing, imaging, microscopy and communication.

In this Review, we concentrate on recent achievements of IR metasurfaces in manipulating the polarization. Here, we select the polarization control as an example in discussing the principle of metasurface-enabled wave manipulation, and note that the discussed principle can be applied to phase and amplitude control. We start by briefly introducing the description of polarization on the standard PS and HOPS, followed by the metasurface-enabled IR polarization manipulation and typical IR polarization-modulated functional meta-devices. Afterward, we discuss metasurface-enabled IR structured light generation and corresponding applications. We then review various strategies for polarization detection on both types of PS. We conclude the Review by discussing the challenges and future directions of the development of IR metasurfaces.

Description of the polarization state

Jones vector and Stokes parameters

The state of polarization (SOP) is an intrinsic property of an electromagnetic wave that characterizes the vectorial nature of the oscillating electric field. The SOP determines how an electromagnetic wave interacts with matter and carries crucial information about the composition and structure of the matter, forming a basis for a variety of optical technologies. To mathematically describe the SOP, the vector form $[E_{x0}e^{i\phi_x},E_{y0}e^{i\phi_y}]^{\mathrm{T}}$ was proposed by Jones in 1941 [79], where E_{x0}, E_{y0} and φ_x, φ_y are respectively the electrical components and phases of a light beam along two axes.. This mathematical description is capable of describing an electric vector with two orthogonal components, however, restricted to fully polarized light.

In 1852, Stokes proposed a set of four parameters to completely characterize the SOP of arbitrarily polarized light (i.e., fully polarized light, partially polarized light or natural light). The Stokes parameters can be expressed with respect to the orthonormal linear polarization bases as

$$S=\begin{bmatrix}S_0\\S_1\\S_2\\S_3\end{bmatrix}=\begin{bmatrix}E_x^2+E_y^2\\E_x^2-E_y^2\\2E_xE_y\cos\phi\\2E_xE_y\sin\phi\end{bmatrix} \quad (1)$$

where E_x and E_y represent respectively the electric field amplitudes of the x and y components and φ is the phase difference between them. The first Stokes parameter S_0 represents the total intensity of the

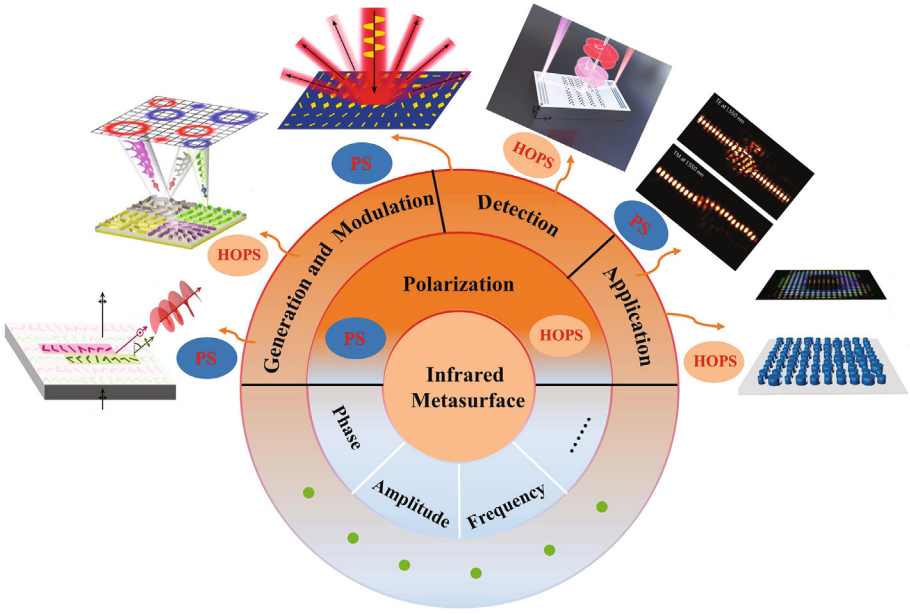

FIGURE 1

Overview of recent developments of IR metasurfaces for polarization control on both the standard and higher-order Poincaré spheres. The symbols 'PS' and 'HOPS' are the abbreviations of Poincaré sphere and higher-order Poincaré spheres, respectively. The ellipsis indicate that the corresponding contents are out of this review.

electric field while the remaining parameters describe the SOP. According to this formula, the polarization can be determined via retrieving the Stokes parameters, which requires a series of intensity measurements [80].

Polarization state on the standard PS and HOPS

In 1982, Poincaré proposed a geometric representation of the SOP now known as the PS, which unifies all the fundamental polarizations that have spatially homogeneous distributions [81]. In this geometric representation, the SOP is mapped to the surface of the PS via the Stokes parameters in the sphere's Cartesian coordinates. Fig. 2(a) shows the polarization states on the standard PS, where the poles represent two circular polarizations (CPs), points on the equator represent linear polarizations, and intermediate points between the poles and equator represent elliptical polarizations. Despite its powerful ability to represent the SOP, the standard PS is limited to describe the scalar beams (i.e., beams with spatially homogeneous polarization). Recently, beams with spatially inhomogeneous polarization have attracted extensive attentions in the fields of optical trapping [82,83], optical microscopy [84], quantum information technology [85] and high capacity optical communication [86,87]. To describe these beams, an extended generalized geometric representation known as the HOPS has been proposed [48,88–90]. Similarly, the corresponding polarization states are mapped to the surface of the HOPS via the higher-order Stokes parameters. Fig. 2(b) shows the polarization states on a specific HOPS, where the poles of the HOPS indicate two circularly polarized vortex beams (with different topological charges). The north pole indicates a right-handed circularly polarized (RCP) vortex beam with topological charge $m = 1$, while the south pole represents a left-handed circularly polarized (LCP) vortex beam with topological charge $n = -1$. Each point on the HOPS can be expressed as a linear superposition of the two circularly polarized vortex beams. The HOPS describes the evolution of both the phase and polarization, providing new degrees of freedoms for polarization-related applications.

Optical properties of common infrared materials

As we know, natural materials are usually composed of atoms or molecules, and their electromagnetic properties depend on the characteristics of their minimum building blocks (e.g., the arrangement of atoms and the forces acting between molecules). For metamaterials, the building blocks are artificially designed structures and thus their electromagnetic properties can thus be set, in theory. Although the geometric parameters play a vital role in the design of metasurface (which are the two-dimensional equivalents of metamaterials), the properties of metasurface are also fundamentally decided by the constituting materials. For example, the intrinsic ohmic loss of metallic structures inevitably restricts the efficiency. Fig. 3 depicts the optical properties of materials commonly used as the building blocks of metasurfaces in IR wavebands, where the refractive index and the optical transparency window of the typical infrared materials are clearly demonstrated [92,93].

As shown in Fig. 3, the silicon material has a low absorption loss ranging from near-IR to the mid-IR till around 8.5 μm [93]. Moreover, with the merits of well-developed fabrication techniques and complementary metal–oxide–semiconductor compatibility, silicon verified to be an attractive choice for near-IR and mid-IR wavebands metasurfaces. Beyond 8.5 μm, germanium is a suitable material for mid-IR wavelengths, owing to its low absorption loss within 2–14 μm. Based on various germanium-based platforms (such as germanium-on-silicon and germanium-on-silicon-on-insulator), mid-IR waveguides have been demonstrated [93]. However, the extension of germanium to metasurfaces needs to be further explored. For the mid-IR

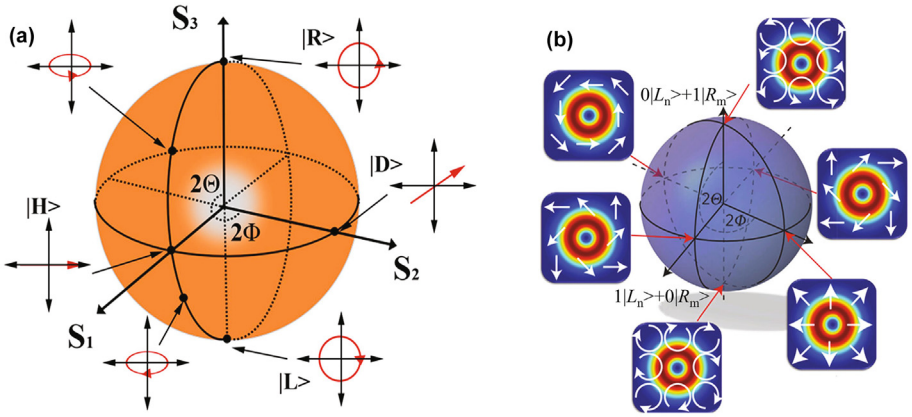

FIGURE 2

Representation of the polarization states on the standard PS and HOPS. (a) Expressions of some typical polarization states at specific positions on the standard PS. Reproduced with permission [90]. (b) Expressions of some typical polarization states at specific positions on a HOPS. Here, the north pole indicates a right-handed circularly polarized vortex beam with topological charge m = 1, while the south pole represents a left-handed circularly polarized vortex beam with topological charge n = -1. Reproduced with permission [91].

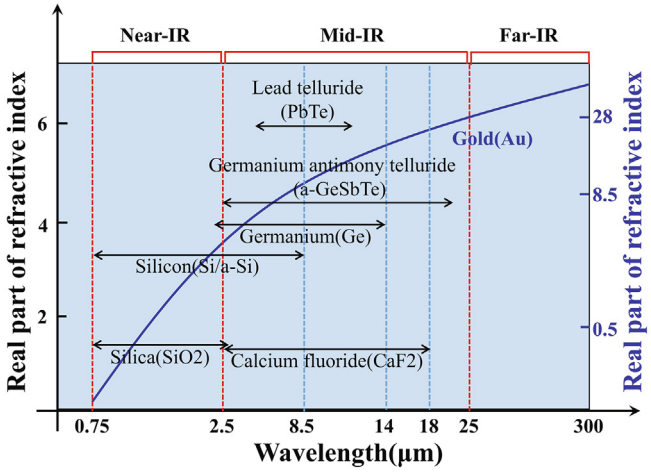

FIGURE 3

Refractive index (real part) of infrared materials commonly used as the building blocks of metasurfaces [92,93]. The double sided arrows along the horizontal axis indicate the optical transparency window. The vertical locations of double sided arrows denote the approximate average refractive index. The solid blue line depicts the refractive index (real part) of gold.

wavebands of 5–10 μm, lead telluride (PbTe) with a refractive index (up to 6) is another choice [62]. Having low absorption loss ranges from 2.5 to 20 μm, amorphous germanium antimony telluride (a-GeSbTe) is a suitable material for the mid-IR wavebands [94]. Furthermore, noble metals such as gold and silver are often used in IR metasurface design [1,20]. The refractive index (real part) of gold ranges from the near-IR to far-IR is shown as a solid blue line in Fig. 3. Despite having very low efficiency, plasmonic metasurfaces own wavefront shaping capacity in the whole IR region. On the other hand, the selection of the substrate is another key issue for high efficiency infrared nanodevices. As shown in Fig. 3, the silica exhibits high absorption loss in the mid-IR waveband and can be replaced with calcium fluoride (CaF2), which owns low absorption loss ranging from 2.5 to 18 μm.

Note that we show the optical transparency window of the typical infrared materials (except gold) in Fig. 3, in which the resulting meta-devices would exhibit high efficiency. In fact, the working bandwidths of these materials could be largely broadened at the sacrifice of efficiency. It is our belief that the discovery of new materials and the rapid development of material synthesis and nano-fabrication techniques will promote intriguing progresses in infrared metasurfaces, facilitating the future development of compact and integrated meta-devices.

IR polarization manipulation on the standard PS

The arbitrary polarization manipulation of light has attracted much attention for its indispensable applications in modern integrated optics. Conventional methods for polarization manipulation (e.g., the use of wave plates) depend on birefringent materials, which accumulate different phase differences along the two orthogonal directions, resulting in bulky configurations and a lack of flexibility. The emerging metasurfaces have overcome this problem, providing a new platform for flexible polarization manipulation on the standard PS. In this section, we review available typical metasurface-enabled strategies proposed for achieving polarization manipulation and polarization-triggered functional meta-devices in the IR region.

IR metasurface-enabled polarization manipulation

To achieve arbitrary polarization evolution on the standard PS, a variety of polarization manipulators have been proposed, such as half-wave plates, quarter-wave plates, and optically activity devices. For these devices, anisotropic nanostructures analogous to conventional birefringent materials are often selected as constituted elements, which are optimized to render equal amplitudes and the targeted phase difference (i.e., π or $\pi/2$ for half-wave plate or quarter-wave plate) under two orthogonal linearly polarized light beams [95–98]. However, these devices are based on the relatively narrow resonance of the constituent elements, which severely restricts their operating bandwidth. Furthermore, the optical background further undermines the performance of these devices. An alternative method that solves these issues is

presented in Fig. 4(a), where two super-cells consist of anisotropic optical antennas. The setup achieves a broadband, background-free quarter-wave plate in the mid-IR waveband of 5–12 μm [20]. Here, the phase gradient in the two super-cells and a $\pi/2$ phase difference between them lead to a deflected circularly polarized beam in the far field, getting rid of the incident background. Utilizing the same design strategy, an polarization manipulator capable of generating scattered light with arbitrary polarization states was later demonstrated based on aluminum metasurface [99]. Despite working in visible bandwidth, such a meta-device can be scaled to the IR band using the same design strategy.

Another important figure of merit in polarization manipulation is efficiency. A common method of achieving high efficiency is to adopt hybrid dielectric–metal or all-dielectric configurations [21,100], while further loss reduction is possible through the engineering the bandgaps of materials [101]. As shown in Fig. 4(b), based on the generalized Huygens principle, a dielectric meta-device is demonstrated which consists of elliptical silicon meta-atoms [21]. Through the overlapping of the scattering contributions from several electric and magnetic multipolar modes, polarization manipulators (i.e., a half-wave plate and quarter-wave plate) with high transmission of about 90% can be achieved over a 100 nm bandwidth with the central wavelength of 1550 nm.

Previous studies on metasurfaces mainly investigated regular shaped structures, which fundamentally limits the shape birefringence and functions. To address this limitation, as shown in Fig. 4(c), an irregular shaped metasurface with angle-tunable arbitrary birefringence has been demonstrated at an operation wavelength of 1550 nm, by using the adjoint-based topological optimization method [102]. With specific birefringence that can be continuously tuned from linear to elliptical birefringence, such a device could expand the scope of polarization optics, indicating compact and versatile polarization operations. Optical activity, usually occurring in the optically active materials, can also be realized in elaborately designed non-chiral metasurfaces [103–105]. Kildishev et al. demonstrated an optically active

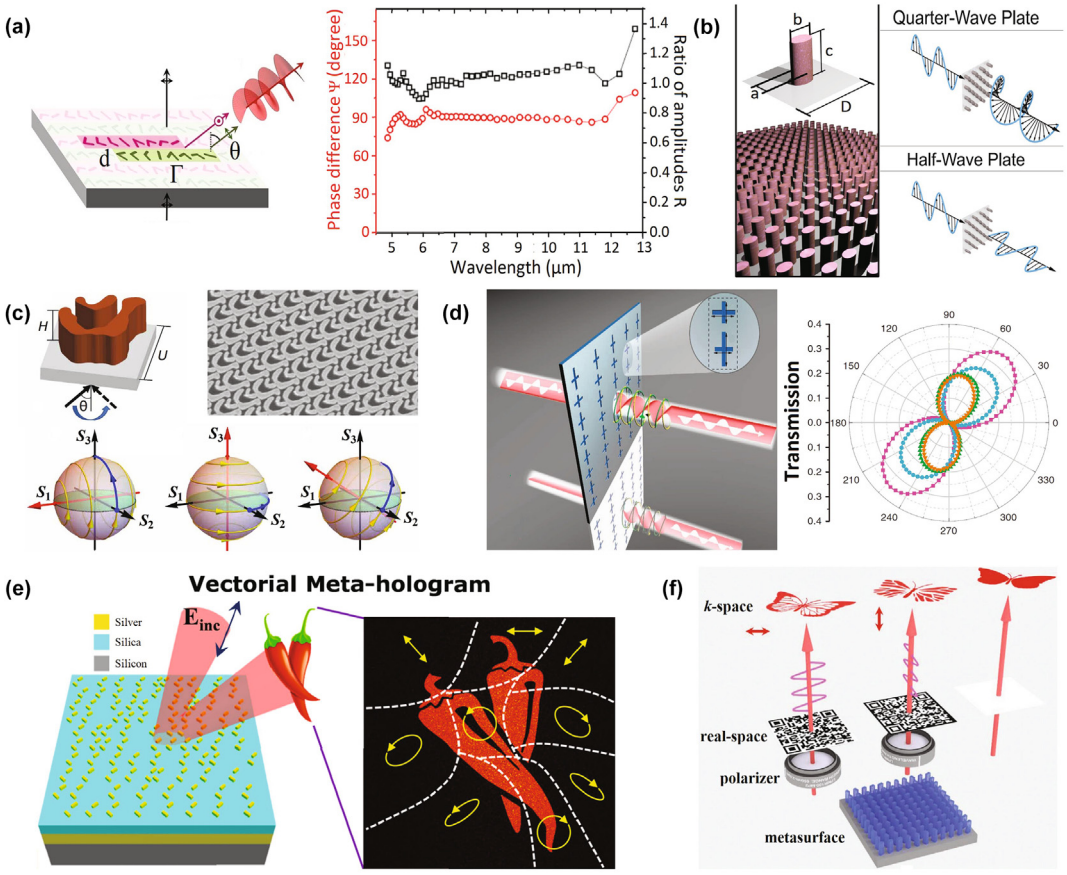

FIGURE 4

IR metasurface-enabled polarization manipulation on the standard PS. (a) Left panel: schematic of the background-free quarter-wave plate composed of two V-shaped super-cells. Right panel: simulated phase shift and ratio of amplitudes between the two orthogonal linearly polarized lights versus wavelength. Reproduced with permission [16]. (b) Schematic of the dielectric meta-device consists of elliptical silicon meta-atoms, which functions as either a broadband half-wave plate or a broadband quarter-wave plate depending on the phase retardance. Reproduced with permission [17]. (c) Schematic of the topology optimized structure element and polarization space representation of linear, circular, and elliptical birefringence. Reproduced with permission [102]. (d) Left panel: schematic of the optical activity device consists of a nonchiral metasurface. Right panel: experimental transmissions versus analyzer angle φ for the designed four samples. Reproduced with permission [104]. (e) Schematic of the metasurface vectorial holography that generates holographic image with arbitrarily spatially varying polarization states. Reproduced with permission [108]. (f) Schematic of the dielectric metasurface capable of encoding a vectorial holographic image in *k*-space and a QR code in real-space. Reproduced with permission [111].

metasurface with non-chiral meta-atoms, which is capable of rotating linearly polarized lights by 45° in the near-IR region [103]. As illustrated in Fig. 4(d), by modulating the phase differences between two sub-units, an optically active metasurface has been shown to continuously control the optically activity from 3° to 42° at a working wavelength of 990 nm [104]. The strategy of utilizing spatially periodically arrayed anisotropic optical meta-atoms has been verified as an efficient and flexible tool for modulating the SOP of incident light. In particular, by hybridizing metasurfaces with functional materials such as phase-change materials, the dynamical manipulation of polarization states in the mid-IR can be realized [106].

Apart from the above-mentioned meta-devices that generate homogeneous polarization profiles, spatially customized polarization manipulation has also been demonstrated in metasurfaces [107]. Here, the definition of vectorial holography was introduced. In contrast to traditional holography, the reconstructed images of vectorial holography possesses a spatially varying polarization profile [108]. Vectorial holography can thus be regarded as a special kind of polarization manipulation on the PS. To date, various metasurface-enabled vectorial holographies have been achieved [40,108–111], which are able to enhance the information capacity and encryption security of holograms owning to the additional polarization degree of freedom. By utilizing diatomic metasurface consisting of two orthogonal silver meta-atoms, Deng et al. demonstrated broadband vectorial holography in the waveband of 670–780 nm [108]. As demonstrated in Fig. 4(e), holographic image with arbitrarily spatially varying polarization states has been achieved, suggesting a new route for information anti-counterfeiting. To enhance the efficiency and information security, metasurface vectorial holography in the momentum space (*k*-space) has been proposed at an operating wavelength of 800 nm [111]. As shown in Fig. 4(f), an all-dielectric configuration is adopted to overcome the absorption loss of silver. The meta-device is capable of showing a grayscale QR image in real space and reconstructing a vectorial holographic image in *k*-space. The polarization states here are identical at the holographic image plane and can be designed to have a customized polarization distribution. This meta-device needs an additional lens for information decryption in *k*-space, further enhancing the security of information encryption.

Polarization-triggered functional meta-devices

The polarization dependence of meta-devices has wide-spread applications in numerous fields, such as optical sensing, imaging, microscopy and communication. To be specific, the polarization dependence can be used to probe the material texture and help defeat camouflage in remote sensing applications [112]. Moreover, polarization sensitivity is also used to enhance the functionality of optical technologies, such as polarization spectroscopy [113], imaging [114], and radar systems [115]. Additionally, polarization-triggered wavefront manipulations are becoming important in engineering functional devices [116–119]. Here, we review some typical IR polarization-modulated meta-devices with unconventional functionalities.

(1) Polarization imaging based on meta-lenses. As we know, the spectral and hyperspectral imaging techniques extract molecular and material composition information of an object. Polarization imaging can extract additional information such as the shape and texture of objects, the optical activity of the materials and the orientation of light emitters, leading to various applications ranging from astronomy and remote sensing to biology [114,120,121]. To date, several infrared polarization cameras based on metasurface have been reported, which are able to complement the conventional bulky polarization imaging systems in many applications [122–125]. Fig. 5(a) shows multidimensional spin-dependent beam splitting using a dielectric polarization-modulated meta-device [122]. By combining the dynamic phase and geometric phase, the meta-device simultaneously realizes longitudinal focusing and transverse shifting at a wavelength of 980 nm, indicating potential applications in spin-controlled nanophotonics. Although the imaging functionality has not been demonstrated, this meta-device could be utilized for polarization imaging. For practical applications, Yan et al. demonstrated an all-silicon meta-device for mid-IR (10.6 μm) active-illumination polarization imaging [123]. Such a meta-device is able to conduct simultaneous real-time imaging under two orthogonal polarization channels, unveiling the potential of compact polarization detection systems. Moreover, chromatic aberration is an important issue that deteriorates the performance of the meta-device. To solve this issue, Ou et al. proposed a mid-IR (3.5–4.75 μm) meta-device to achieve polarization-controlled broadband achromatic focusing and focusing vortex, as shown in Fig. 5(b) [124]. The meta-device is comprised of an all-silicon metasurface that is compatible with silicon-based semiconductor manufacturing, enabling applications in polarization imaging, and multidimensional display.

(2) Polarization-modulated meta-holography. Holography invented by Gabor provides a promising technology for restoring and reconstructing the full wave information of target objects. Adding an additional modulation degree of freedom such as polarization to holography could enhance the information capacity and security of information encryption. Fig. 5(c) shows polarization-multiplexed holography operating at a wavelength of 915 nm, where different images are reconstructed under two orthogonal linearly polarized (*x*- and *y*-polarized) light beams [76]. Other applications, such as polarization conversion and polarization-controlled holography, can be carried out using a simple system [126]. In the realization of such a meta-device, the Gerchberg-Saxton (G-S) algorithm is adopted to encode two independent phase profiles for the two polarizations. Such a holography strategy can also be applied to CP polarizations. As shown in Fig. 5(d), two different images can be reconstructed via switching the helicity of the incident light in a broad wavelength ranging from1100 to 1800 nm [127].

(3) Polarization-modulated on-chip meta-devices. Adopting the inverse design optimization method, Shen et al. demonstrated a polarization-selective waveguide mode splitter with a footprint of 2.4 μm × 2.4 μm [128]. The designed polarization mode splitter is shown in Fig. 5(e), where different incident waveguide modes (i.e., transverse electric and transverse magnetic modes) are directed to different waveguide branches at an operating wavelength of 1550 nm. Zhou et al. presented an ultra-compact on-chip broadband polarization diversity orbital angular momentum (OAM) generator composed of a superposed

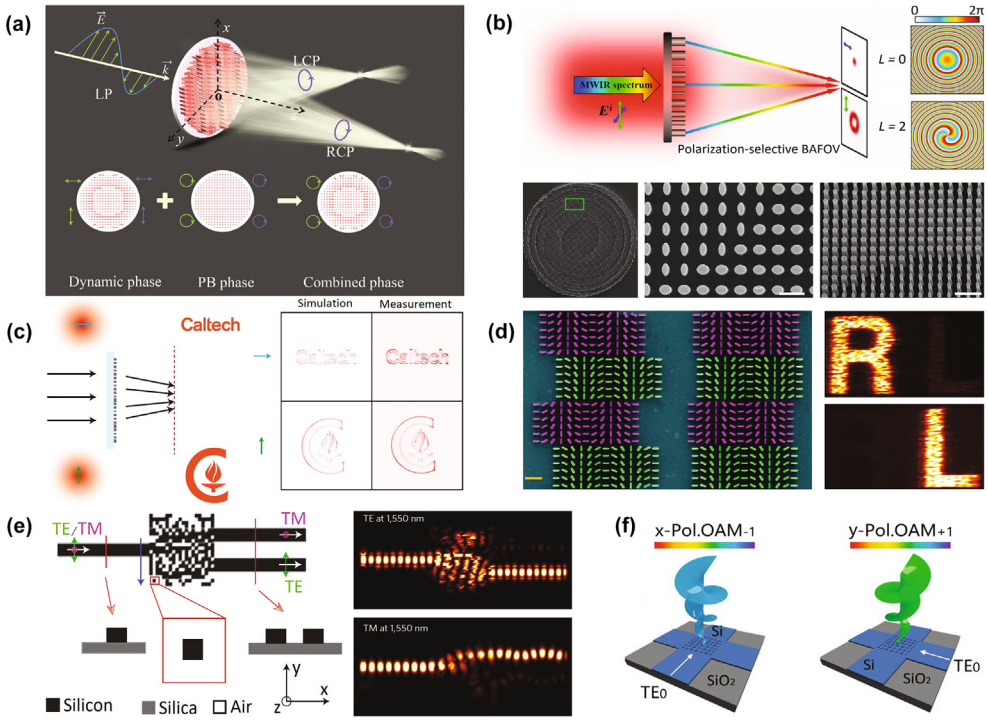

FIGURE 5

Polarization-modulated IR functional meta-devices. (a) Schematic of the meta-device for multidimensional manipulation of the photonic spin-Hall effect, in which spin-dependent transverse shifting and longitudinal focusing are realized. Reproduced with permission [122]. (b) Upper panel: schematic of the polarization-selective broadband achromatic focusing optical vortex generator, which generates achromatic focusing with different topological charge numbers. Lower panel: SEM images of the fabricated polarization-controlled meta-device. Reproduced with permission [124]. (c) Schematic of the polarization-multiplexed dielectric metasurface that generates two different holograms under two orthogonal linearly polarized (*x*- and *y*-polarized) lights. Reproduced with permission [76]. (d) SEM image of the helicity-multiplexed meta-hologram and the corresponding results under RCP and LCP incident lights. Reproduced with permission [127]. (e) Left panel: schematic of the on-chip polarization beam splitter. Right panel: functionality of the polarization beam splitter that separates the TE and TM beams into two waveguide branches. Reproduced with permission [128]. (f) Schematic of the on-chip broadband polarization diversity vortex beams generator consisting of superposed holographic fork grating on a silicon waveguide, which generates *x*-polarized OAM_{-1} and *y*-polarized OAM_{+1}. Reproduced with permission [129].

holographic fork grating patterned on top of a silicon waveguide. Such an on-chip device can generate four polarization diversity OAM modes within a wavelength band from 1500 to 1630 nm, with two of the modes (*x*-polarized OAM_{-1} and *y*-polarized OAM_{+1}) shown in Fig. 5(f) [129]. Moreover, polarization modulated functional meta-devices have been also demonstrated in full spaces by using cascaded and single-layer metasurfaces [130,131].

IR polarization manipulation on the HOPS

Metasurface-enabled structured light

Structured light beams have shaped spatial structures, such as inhomogeneous amplitude, phase and polarization distributions [132]. The facilitation of various applications with structured light requires the flexible generation and manipulation of structured light on the HOPS. A large number of conventional schemes have been demonstrated for structured light generation and manipulation, such as the spiral phase plate, q-plate, cylindrical lens pairs and spatial light modulator [133–136]. However, these configurations are bulky, hindering the development of integrated optical devices. The use of metasurfaces can overcome this problem.

With properly designed meta-atoms, a metasurface can flexibly generate structured light beams from transmission mode to reflection mode, from single OAM to multi-OAMs, from discrete OAMs to arrayed OAMs, and from free space to on-chip configuration [1,45,47,100,137–150]. Fig. 6(a) demonstrates a vortex beam generator consisting of eight regions, which are designed to impart an azimuthally varying phase from 0 to 2π [1]. Under plane wave illumination, an optical vortex with topological charge of $l = 1$ is generated within a broad band from 5 to10 μm. The topological charge can be identified by its interference with a titled Gaussian plane beam or a co-propagating Gaussian spherical beam. To improve the relatively low efficiency of the plasmonic devices, as shown in Fig. 6(b), a hybrid dielectric-metal configuration has been introduced [100]. The generated cross-polarized vortex beam owns high efficiency over a waveband of 1500 to 1600 nm. Another common method to improve the efficiency is the adoption of Huygens' metasurface, and a transmission efficiency exceeding 70% is achieved using silicon nanodisks [140].

Using the gradient-rotation split-ring antennas, separated OAMs with opposite topological charge are achieved in a broad wavelength band [142]. However, this scheme is restricted to CPs and opposite topological charges are generated [150]. To solve this issue, Capasso et al. proposed a completely new OAM generation tool—the J-plate, which provides unprecedented control over the total OAM in the visible waveband

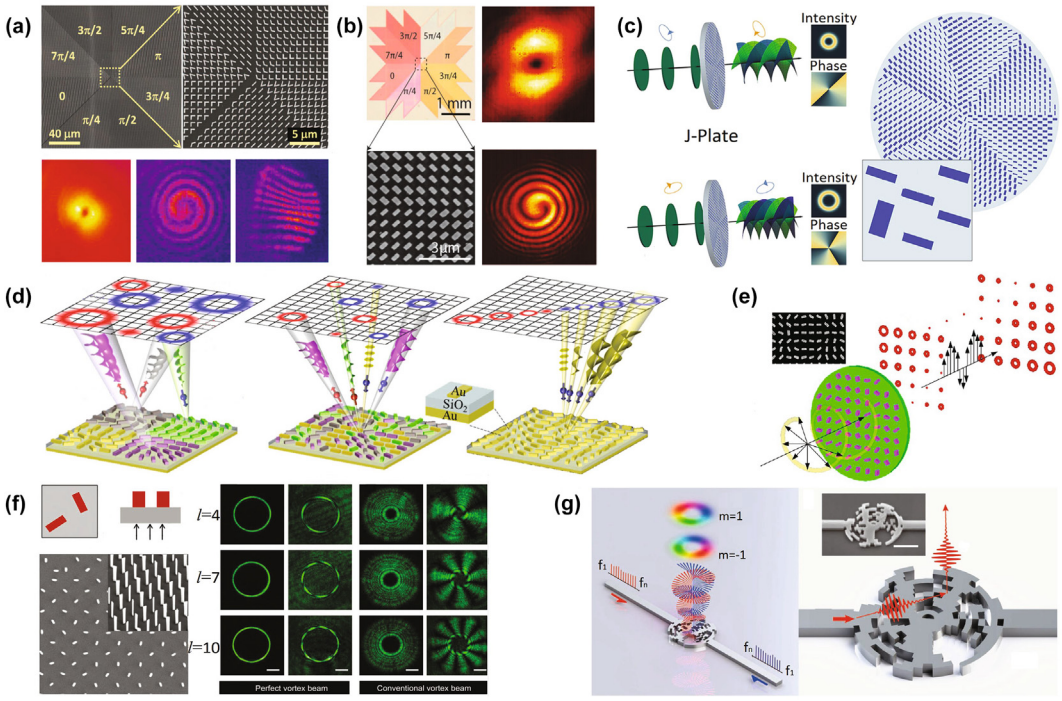

FIGURE 6

Structured light generation based on metasurfaces. (a) SEM image of the plasmonic vortex beam generator and the measured far-field intensity profiles (from left to right corresponding to the vortex beam intensity distribution, the interference pattern with a co-propagating Gaussian beam and the interference pattern with a tilted Gaussian beam). Reproduced with permission [1]. (b) SEM image of the hybrid dielectric-metal metasurface and the measured far-field intensity profiles. Reproduced with permission [100]. (c) Schematic and operating concept of the J-plate that converts an arbitrary pair of orthogonal polarization states into two beams with independent values of topological charge. Reproduced with permission [149]. (d) Schematic of the three typical shared-aperture design concepts (segmented, interleaved and harmonic resonance) and far-field intensity profiles with positive (red) and negative (blue) helicities emerging from the metasurfaces. Reproduced with permission [141]. (e) Schematic of the creation and reconstruction process of a 3D vortex array based on a dielectric metasurface. Reproduced with permission [143]. (f) Left panel: the schematic and SEM image of the metasurface with independently amplitude–phase modulation. Right panel: measured cross-polarized and interference intensity distributions of the perfect vector vortex beam with various topological charges. Reproduced with permission [47]. (g) Schematic of a silicon-based OAM emitter, which could emit coaxial OAM beams across a broad bandwidth. Reproduced with permission [147].

[149]. The schematic of J-plate is shown in Fig. 6(c), which overcomes the polarization restriction and is capable of converting an arbitrary pair of orthogonal polarization states into their conjugate states, creating two OAMs with independent topological charges. Using this design strategy, a novel analogous vortex beam generator can be realized in the IR region. For generating multi-OAMs via a single metasurface, the structure multiplexing strategy is adopted. As shown in Fig. 6(d), Maguid et al. summarized three multiplexing strategies (i.e., the segmented strategy, interleaved strategy and harmonic resonance strategy), all of which are capable of creating several independent vortex beams with different topological charges [141]. Moreover, as shown in Fig. 6(e), a three-dimensional optical vortex array with equal intensity and micrometer spatial separation has been achieved at an operation wavelength of 780 nm by combining the principles of Dammann gratings and Dammann zone plate [143]. On the other hand, perfect vortex beams have annular intensity profiles that are independent of topological charges, and have promising applications in particle manipulation and fiber communication [46,151]. As shown in Fig. 6(f), Qiu et al. proposed a single-layered metasurface, whose unit cell consists of two identical meta-atoms, for the arbitrary and full control of perfect vector vortex beams [47]. Therein, using a genetic algorithm, four parameters (positions and rotated angles) are optimized to obtain independent and arbitrary control over the amplitude, phase and polarization of light.

Moreover, other typical structured beams like Bessel beams and Airy beams have been generated using metasurfaces [117,152–154]. With the properties of non-diffraction propagation and self-healing, these beams have potential applications in laser fabrication, imaging and optical manipulation. Here, we concentrate on the generation of polarization-controlled Bessel beams and Airy beams using infrared metasurfaces [155,156]. Guo et al. demonstrated the generation of a polarization-controlled broadband Airy beam at waveband from 532 to 780 nm via a single catenary-shaped metasurface [155]. The spatially continuous catenary meta-atoms exhibit great advantages of broadband and high efficiency over their discrete counterparts. Combining the geometric phase and dynamic phase, Li et al. proposed a compact all-dielectric metasurface operating at a wavelength of 1550 nm, with the ability to convert any two orthogonal polarizations to independent Bessel beams [156]. The polarization-controlled structured-beam generation would promise applications in multifunctional devices.

Besides the unprecedented capacity of generating structured light in free space, metasurfaces also allow the generation of

structured light on an integrated chip. Yu et al. demonstrated a silicon integrated vortex laser emitter with well-controlled OAM at a working wavelength of 1550 nm. They used an angular grating sidewall to scatter whispering-gallery-mode light into free-space vortex beams [137]. Despite its compact footprint and accurate phase control, the resonant feature of whispering gallery modes inevitably leads to a narrow bandwidth. To overcome this restriction, Yuan et al. proposed an ultra-broadband multiplexed on-chip OAM emitter as shown in Fig. 6(g), using the inverse design optimization method [147]. This emitter owns a micron-sized radius and is capable of emitting coaxial OAM beams across a broad bandwidth from 1450 to 1650 nm.

Structured-light-empowered applications

With the development of nano-fabrication technology, various metasurface-enabled schemes for flexibly generating and manipulating structured light have been developed, empowering ever growing applications in various fields. In this subsection, we review several typical applications of structured light, such as micro-particle trapping, image processing of edge detection, OAM or cylindrical vector beams (CVB)-multiplexed high-capacity information communication.

In the past few years, structured light beams have been utilized for micro-particle trapping and manipulation, providing unprecedented localization accuracy that exceeds that provided by standard beams [157–161]. As demonstrated in Fig. 7(a), Zhang et al. proposed a wide-angle (from −50° to 50°) beam steering meta-device operating at a wavelength of 1550 nm for optical particle trapping. The meta-device consists of two blazed gratings, and converts the input beam to a beam that has an intensity gradient, which is appropriate for particle trapping. Very recently, a highly efficient optical tweezer setup based on silicon-based vortex metalens for two-dimensional optical trapping has been demonstrated at a working wavelength of 800 nm, as shown in Fig. 7(b). This versatile optical tweezer setup allows polarization-sensitive particle manipulation without using additional conventional optical elements [161].

Thanks to their unique spatially inhomogeneous polarization distributions in tight focusing, CVBs can be used for optical data storage. As shown in Fig. 7(c), massively-encoded optical data storage can be achieved in tightly focused segmented CVBs (at a wavelength of 950 nm), by harnessing the multichannel information encoding and decoding during the light-matter interactions [162]. Recently, an OAM beam has been utilized to perform optical spatial differentiation computing, showing potential applications in the image processing of edge detection [163–165]. Fig. 7(d) represents the schematic of a meta-device with spin-dependent switching between bright-field imaging and edge-enhanced contrast imaging in the visible waveband [166]. To obtain two-dimensional spatial differentiation operation for isotropic edge detection, a Fourier transform setup is incorporated with the spin-multiplexing all-dielectric

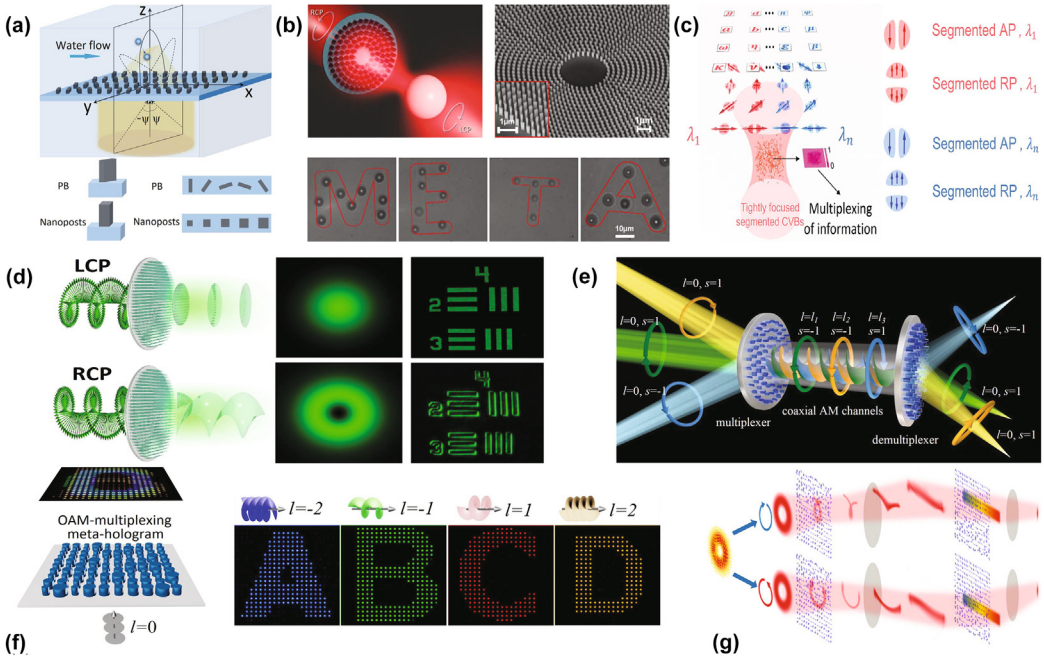

FIGURE 7

Structured-light-empowered applications. (a) Schematic of the wide-angle beam steering meta-device for optical particles trapping. Reproduced with permission [160]. (b) Upper panel: conceptual image illustrates the trapping of a polystyrene microbead and SEM image of the all dielectric metalens. Lower panel: polystyrene particles with different diameters dispersed in water and arranged by polarization-sensitive drag and drop. Reproduced with permission [161]. (c) Left panel: principle of multi-dimensional optical data storage using tight focusing segmented CVBs. Right panel: the two-lobe profiles indicate the segmented azimuthally polarized and radially polarized beams produced by a linear polarizer. Reproduced with permission [162]. (d) Schematic of the spin-multiplexed metasurface that achieves spin-dependent switching between bright-field imaging and edge-enhanced contrast imaging. Reproduced with permission [166]. (e) Schematic of the AM multiplexing and demultiplexing using all-dielctric metasurface. Reproduced with permission [167]. (f) Schematic of the OAM-multiplexed meta-hologram which is able to reconstruct multiple distinctive OAM-dependent holographic images. Reproduced with permission [171]. (g) Schematic of the coaxial CVB sorting based on the spin-dependent optical geometric transformation that converts the LCP and RCP components to two spots. Reproduced with permission [87].

metasurface. This meta-device can be scaled to the IR waveband with the same design strategy.

To date, OAMs and CVBs, have been shown to be effective in high-capacity information communication owing to their physically unbounded set of orthogonal modes [38,87,167–171]. As shown in Fig. 7(e), an angular momentum (AM) multiplexing and demultiplexing scheme based on all-dielectric metasurfaces at operating wavelength of 1310 nm has been demonstrated [167]. The off-axis technique is adopted for the OAM multiplexing/demultiplexing functionality. To function as an spin angular momentum (SAM) multiplexer/demultiplexer, the photonic spin Hall effect is utilized in the anisotropic medium. The designed meta-device owns ten AM multiplexing/demultiplexing channels and exhibits excellent performance (with a demultiplexing efficiency for each channel up to 8% and a maximum crosstalk of −12.8 dB). Despite the variety of previous reports on OAMs, however, most OAMs have never been used as independent information carriers in holography by 2020, due to the lack of OAM selectivity. Very recently, the metasurface-based OAM holography has been introduced. The key to this holography is to conduct the OAM-dependent spatial sampling of the digital hologram. As shown in Fig. 7(f), OAM-multiplexed holography is achieved with different holographic images being reconstructed from the same metasurface using specific OAMs. The holography has promising applications in high-capacity three-dimensional display and high-security encryption [171]. However, such an OAM-holography is based on a phase-only strategy, which suffers from channel crosstalk so that only four multiplex channels have been achieved. To solve these issues, a complex-amplitude metasurface in momentum space has been proposed. This metasurface has independent and complete control over the amplitude and phase, and the number of the multiplex channels has thereby been increased to 200 [172]. In view of their specific characteristics, CVBs are also treated as promising candidates for multiplexing optical communication. Yuan et al. demonstrated a CVB multiplexing communication system in both a few-mode optical fiber and free space at a wavelength of 1550 nm [Fig. 7(g)], showing the potential to further increase the current state-of-art communication capacity by one or two orders of magnitude [87].

IR polarization detection

As discussed in Sections “IR polarization manipulation on the standard PS” and “IR polarization manipulation on the HOPS”, the generation and manipulation of polarization on both standard the PS and HOPS have important applications in numerous fields. Therefore, detecting the polarization state in a compact and reliable manner is another important topic. However, in conventional polarimetry systems, a series of cascaded optical components (e.g., wave-plates, polarizers, and diffractive fork gratings) are necessary for polarization detection, severely hindering the future applications of the systems to integrated devices. The emergence of metasurfaces appears to provide an effective way to cope with this problem. In this section, we review the metasurface-enabled IR polarimetry setups, aiming at accurately detecting light polarization on both the standard PS and HOPS.

Principles for detecting light polarization

Due to the lack of a straightforward strategy to probe the phase information, direct polarization detection is challenging. For a fundamental light beam on the standard PS, polarization detection can be transformed into a process of solving the Stokes parameters. From Eq. (1), one can see that the Stokes parameters can be accurately retrieved via a series of intensity measurements. Similarly, for an arbitrary beam on the HOPS, polarization detection can be transformed into the problem of solving the higher-order Stokes parameters [48,88,89,91,173]. For a paraxial beam on the HOPS, the high-order Stokes parameters in the Cartesian coordinates of the sphere can be expressed as

$$S^{m,n}=\begin{bmatrix}S_0^{m,n}\\S_1^{m,n}\\S_2^{m,n}\\S_3^{m,n}\end{bmatrix}=\begin{bmatrix}|A_R^m|^2+|A_L^n|^2\\2|A_R^m||A_L^n|\cos(\phi)\\2|A_R^m||A_L^n|\sin(\phi)\\|A_R^m|^2-|A_L^n|^2\end{bmatrix} \quad (2)$$

where $A_R^m$and $A_L^n$are the amplitudes of the RCP and LCP vortex beams, respectively. Correspondingly,$\phi=\arg(A_R^m)-\arg(A_L^n)$ is the phase difference between the two vortex beams. The Jones vectors of RCP and LCP vortex beams can be expressed as $|R_m\rangle=\exp(im\varphi)(\hat{x}-i\hat{y})/\sqrt{2}$and $|L_n\rangle=\exp(in\varphi)(\hat{x}+i\hat{y})/\sqrt{2}$, where m and n represent the topological charges, σ is the spin of the photon, $\hat{x}$ and $\hat{y}$ represent the unit vectors along x and y axes. Therefore, to fully determine beams on a HOPS, optical singularity associated with angular momentum (σ, m, n) and higher-order Stokes parameters in Eq. (2) should be measured.

Polarization detection on the standard PS

Rapid advances on optical metasurfaces have facilitated the development of a series of conceptually new strategies to partially or completely characterize the polarization [174–186]. Although different metasurface-based setups are introduced in these strategies, they share a common goal, namely, the retrieving of the Stokes parameters partially or completely. Considerable effort has been made to partially resolve light polarization. By designing specific chirality-coded meta-apertures, the handedness of the incident CP light can be resolved over a broad spectral range from 600 to 900 nm [175]. The schematic of the meta-apertures is depicted in Fig. 8(a). The breaking of the spin degeneracy results in a spin producing opposite transmission spectra. Besides the helicity, other parameters can also be detected for polarization characterization. Wei et al. recently demonstrated a mid-IR metasurface-mediated graphene photodetector for the calibration-free detection of the polarization angle [181]. Using this meta-device, the polarization angle is unambiguously detected through measuring the vectorial photocurrent induced by the photovoltaic effect. Because of the directionality of the photocurrent and the symmetry of the device, the polarization angle of incident light can be determined via a single measurement of the photocurrent. This measurement is not affected by the intensity, unpolarized component and circularly polarized component of the incident light. Such a strategy can be further extended to measure other optical properties of incident light, such as wavelength, SAM and OAM.

Other metasurface-based setups for partially polarization resolving have been proposed and are not limited to resolving the helicity or polarization angle. Yang et al. proposed a

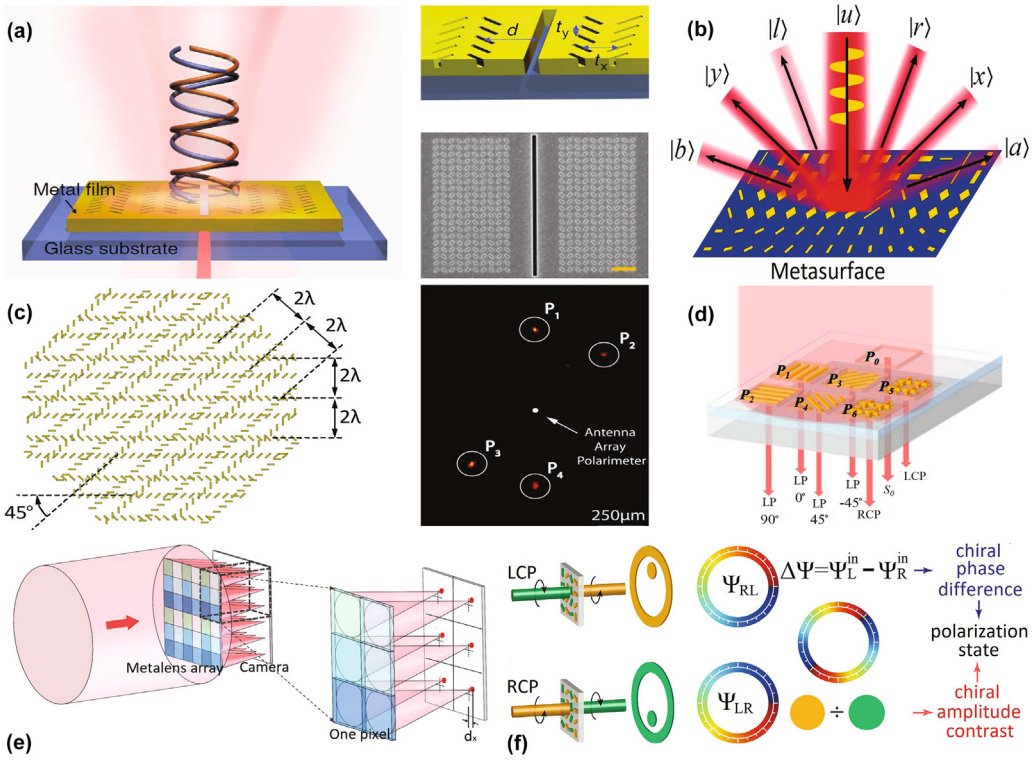

FIGURE 8

IR metasurfaces for partially or fully polarization resolving on the standard PS. (a) Schematic and SEM images of the chirality-coded meta-apertures for photonic spin resolving. Reproduced with permission [175]. (b) Operating principle of the plasmonic meta-grating: spatially diffracting the incident light into six different directions and the Stokes parameters can be retrieved by measuring the intensity contrast. Reproduced with permission [176]. (c) Left panel: schematic of the in-line polarimeter composed of two pairs of gold antenna rows with a separation of 2λ. Right panel: measured intensity profile of the out-coupling gratings. Reproduced with permission [177]. (d) Schematic of the mid-IR meat-device consisting of seven super cells for direct Stokes parameter measurement. Reproduced with permission [187]. (e) Schematic of the generalized Hartmann–Shack sensor consists of six dielectric metalens sub-arrays. Reproduced with permission [188]. (f) Illustration of the concept for holographic polarimetry: the polarization state can be resolved by recognizing the chiral amplitude and chiral phase difference contrasts. Reproduced with permission [180].

meta-device composed of two CP-dependent metalenses, and is capable of resolving the helicity and ellipticity of the incident light over a broad waveband from 1350 to 1750 nm [178]. The ellipticity can be accurately obtained by extracting the focusing efficiency contrast of the two CP-dependent metalenses. Moreover, on the basis of the superposition of vortex beams, polarization parameters such as handedness, the major axis and ellipticity can be detected using a metasurface-based configuration [183]. The major axis and ellipticity of the incident light can be detected by identifying the interference patterns of two vortex beams with identical topological charges but opposite signs, while the handedness can be determined with different topological charges.

To completely resolve polarization, all four Stokes parameters should be retrieved. Fig. 8(b) illustrates the operating principle of a meta-grating enabled polarimeter that operate at a wavelength of 800 nm, and composed of three elaborately designed phase-gradient metasurfaces [176]. For an arbitrary incident light beam, the polarization components are spatially diffracted into six different directions. The four Stokes parameters can be retrieved by simultaneously measuring the far-field diffraction intensities. As shown in Fig. 8(c), a compact in-line polarimeter with an operating wavelength of 1550 nm was proposed, which consists of two pairs of gold antenna rows with a relative angle of 45° [177]. Four specific elliptical polarization components of the incident light are directionally scattered and the polarization can be precisely detected by measuring the far-field intensities in the four scattering directions. Bai et al. demonstrates a chip-integrated meta-device for polarization detection at a mid-infrared wavelength of 3.8 μm [187]. As shown in Fig. 8(d), seven vertically stacked plasmonic metasurfaces are elaborately designed that function as specific polarization filters. The Stokes parameters can be calculated by directly measuring the scattering intensities from the seven polarization filters. Additionally, an elaborately designed metalens has a polarization-dependent focusing effect and can be used to resolve polarization. Fig. 8(e) demonstrates a generalized Hartmann-Shack array of dielectric metalenses operating at a wavelength of 1550 nm, which allows for the real-time determination of the polarization profile of an incident light beam [188]. This meta-device composed of multiple pixels, each of which functions as a polarization-dependent metalens, efficiently focusing the six polarization components to the detector plane. By measuring the focusing intensities of the six polarization components and carefully calibrating the system, the Stokes parameters of an arbitrary light can be accurately retrieved. Moreover, such a device can be utilized to determine the phase profile of a beam on the HOPS thanks to its capacity of simultaneously detecting the phase-gradient profile by

analyzing the displacement of the foci. To fully determine the Stokes parameters, at least four polarization components are necessary [179,189]. Therefore, the pixels of the meta-device in Fig. 8 (e) are simplified by four metalenses capable of focusing four specific polarization components to the detector surface [182]. Apart from meta-grating and metalens, the polarization-dependent hologram has also been utilized for polarization detection. Fig. 8(f) shows the schematic of the holographic polarimeter, which is constructed of a CP multiplexed P-B phase metasurface and could directly detect polarization in a single measurement [180]. This holographic polarimeter shows elegant performance in a broadband spectral range from 580 to 940 nm. Here, the phase difference can be directly read from the holographic image, exhibiting essential difference from other polarimetry setups discussed above.

Polarization detection on a HOPS

To fully determine a beam on a HOPS, the optical singularity associated with angular momentum (σ, m, n) and higher-order Stokes parameters in Eq. (2) should be measured. In conventional polarimetry systems, beams on the HOPS can be resolved by rotating wave-plate or polarizer, but such setups are bulky and difficult to be use in high-speed communication systems. To solve this issue, substantial efforts have been made to develop metasurface-based setups, however, most of them are restricted to partially resolving beams on a HOPS. Up to now, such a technology is not yet mature, and most of the reported metasurface-based setups do not operate at IR wavelengths. Here, we review the primary strategies for partially or fully resolving beams on the HOPSs, regardless of the operating wavelength.

Fig. 9(a) shows the schematic of an on-chip OAM mode detector, which consists of multiple semi-ring plasmonic nanoslits that enhance the intensity for easy measurement [190]. Under a specific circularly polarized vortex beam with topological charge l, the semi-ring plasmonic nanoslit imparted with an azimuthal phase $2l\pi$ functions as a semi-circular source. This nanoslit is therefore capable of spatially sorting various OAM modes of light into different focal spots with a mode interval of about 120 nm. Chen et al. proposed an on-chip plasmonic nanograting that couples the OAM modes into two separated surface plasmon polariton beams with different splitting angles that depend on the OAM modes. The incident OAM modes can be determined from the splitting angles [191]. As shown in Fig. 9(b), Yang et al. proposed a metasurface strategy capable of achieving near-field OAM generation and detection [192]. Combining the circular arrayed specific chirality-coded meta-apertures with the Archimedes-spiral-arrayed cross-shaped apertures, the setup simultaneously resolves the spin of the photon and the OAM modes of the incident CP light.

However, the above devices rely on an accurate alignment that requires tedious adjustment, hindering their practical application. To overcome this disadvantage, optical gratings have been adopted and verified to be excellent choices. For the previous demonstrated on-chip OAM mode detector, the spatial interval is limited by the planar focal length of the semi-ring to as small as 120 nm [190]. To enhance the spatial interval between two adjacent modes and eliminate the need for accurate alignment, a meta-grating constructed of phase-modulated nanoslit arrays has been proposed to detect both the spin and orbital components [193]. As depicted in Fig. 9(c), such a device couples the OAM modes into non-diffracting surface plasmonic beams,

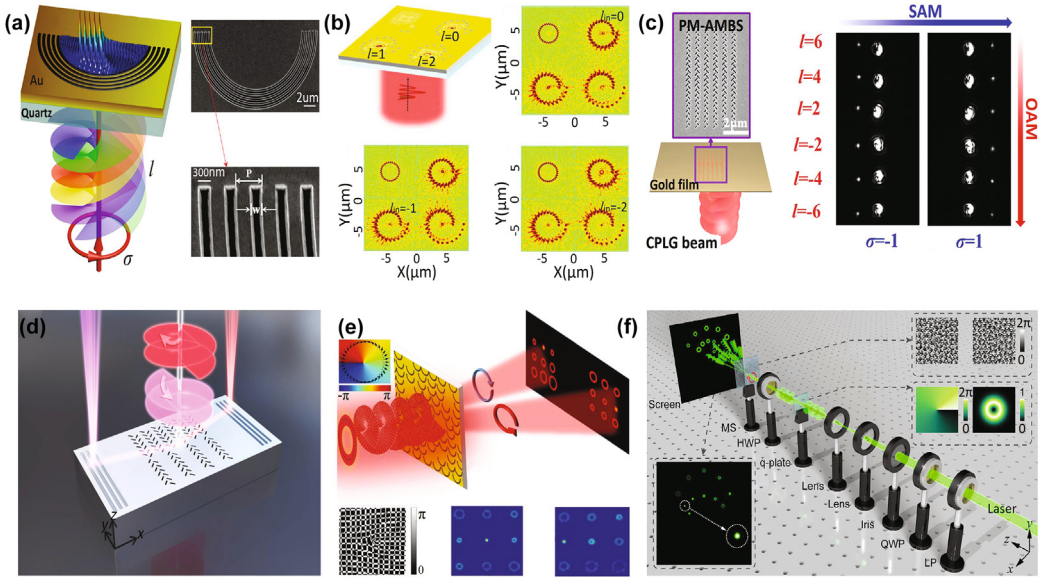

FIGURE 9

Resolving the polarization of beams on a HOPS using metasurfaces. (a) Schematic and SEM image of an on-chip OAM mode detector composed of multiple semi-ring plasmonic nanoslits. Reproduced with permission [190]. (b) Schematic and simulated intensity profiles of the plasmonic OAM detector under LCP vortex beam with different topological charges. Reproduced with permission [192]. (c) Left panel: schematic and SEM image of the phase modulation OAM beam splitter. Right panel: Scattered intensity profiles of the device for incident beams with various angular momentum. Reproduced with permission [193]. (d) Schematic of the plasmonic spin-Hall nanograting illuminated by two beams with different angular momentum. Reproduced with permission [194]. (e) Schematic illustration and simulated results for determining the optical singularities based on the spin-multiplexed metasurface. Reproduced with permission [195]. (f) Schematic of the experimental setup for free space optical singularities determination. Reproduced with permission [196].

and it can detect the OAM modes with a spatial interval lager than 1.1 μm (with a topological charge interval of 2). Very recently, based on a spin-Hall meta-grating [194], an on-chip plasmonic optical vortex detector was proposed, as shown in Fig. 9(d). The vortex detector is sensitive to the spin of the incoming beam and simultaneously determines the polarization and phase singularities. Besides the on-chip metasurface setups, a number of setups have also been proposed in free space to resolve the optical singularity of incident beams [144,195–197]. As shown in Fig. 9(e), using a spin-multiplexed metasurface setup, an alternative strategy for fully detecting the optical singularities (phase and polarization singularities) in free space has been proposed [195]. Therein, the spin-multiplexed metasurface is composed of two segmented and elaborately designed C-shaped apertures, which guides the orthogonal CP components to opposite diffraction directions. Moreover, the two-dimensional Dammann vortex grating is adopted to create spin-dependent optical vortex arrays for singularity detection. However, the ohmic loss of metal results in a very low efficiency. To address this problem, an all-dielectric metasurface has been designed [Fig. 9(f)], which owns the ability to simultaneously detect multiple SAM and OAM modes in a broad waveband [196]. In contrast with the former setup that resolves the chirality adopting the segmented strategy, a harmonic resonance strategy has been adopted to design a helicity-decoupled metasurface [198]. Despite the afore-mentioned achievements accomplished in SAM and OAM modes detection, these setups cannot fully resolve the beams on a HOPS because they are unable to fully determine the high-order Stokes parameters. To fully resolve beams on a HOPS, Yang et al. numerically proposed a single-layer all-silicon meta-device [90]. This meta-device consists of a CP-decoupled focusing vortex generator and four elaborately designed distinctive metalenses and is capable of fully resolving beams on a HOPS with order up to four. Moreover, it is worth mentioning again the generalized Hartmann-Shack array shown in Fig. 8(f), with which one can fully resolve arbitrary beams on a HOPS [182,188]. We believe that the rapid advance of metasurface technologies will would bring about various new planar meta-devices capable of fully resolving beams on the HOPS.

Summary and outlook

In summary, metasurface has been manifested as a promising platform for efficiently controlling the light polarization owing to its capacity in electromagnetic wave manipulation within sub-wavelength scale. Here, we reviewed recent achievements on metasurface-enabled polarization in the IR band. We have presented the schemes and summarized typical strategies for polarization generation, manipulation and detection on the standard PS and HOPS. Correspondingly, various polarization-related applications such as polarization convectors, polarization-multiplexed meta-devices, micro particle trapping, OAM/CVB-multiplexed communications and edge imaging were introduced. To visualize the IR polarization nanodevices, we have put together in Table 1 an overview of their characteristics. Here, the device type, the constituent materials, fabrication techniques, working wavelengths and efficiencies of typical polarization nanodevices are compared.

We believe that the rapid development in nano-fabrication techniques will promote intriguing progresses in metasurfaces whatever their wavelengths, facilitating future design of compact and integrated meta-devices. In particular, IR metasurface-enabled polarization meta-devices can be easily integrated with related systems and have important applications in various fields such as polarization remote sensing, biomedical molecule imaging and diagnosis, and machine vision. Moreover, by utilizing smart materials such as the emerging low-dimensional nanomaterials [5,199,200] with ingenious strategies, the metasurface-enabled polarization generation, manipulation and detection on a HOPS will be constantly improved, facilitating numerous applications such as optical microscopy, quantum information technology, and high-capacity optical communication. Another promising future direction of research is to extend the IR polarization control from linear to nonlinear regimes [201–203].

TABLE 1

Summary of typical metasurface-enabled infrared compact polarization nanodevices.

Type	Polarization nanodevice	Wavelength (μm)	Material	Fabrication techniques	Operation mode	Efficiency	Reference
PS	Quarter-wave plate	5–12	Gold	EBL	T	10%	[20]
	Half-wave plate	1.55	Silicon	EBL	T	80%	[104]
	Polarization rotator	0.99	Air-cut on silver	FIB	T	40%	[104]
	Achromatic metalens	3.5–4.75	Silicon	EBL	T	-	[124]
	Meta-hologram	0.915	Silicon	EBL	T	84%	[76]
	Mode splitter	1.55	Silicon	EBL	On-chip	70%	[128]
	Chirality recognizer	0.6–0.9	Air-cut on gold	FIB	T	15%	[175]
	Polarimeter	0.8	Gold	EBL	R	-	[176]
	Holographic polarimeter	0.58–0.94	Gold	EBL	T	0.23%	[180]
HOPS	OAM generator	5–10	Gold	EBL	T	-	[1]
	OAM generator	1.5–1.6	Silicon	EBL	R	83%	[100]
	OAM emitter	1.45–1.65	Silicon	EBL	On-chip	35%	[147]
	Optical tweezer	0.8	Silicon	EBL	T	-	[161]
	OAM multiplexer/ demultiplexer	1.31	Silicon	EBL	T	80%	[167]
	Singularity detector	0.98	Air-cut on gold	FIB	On-chip	-	[193]
	Polarimeter	1.55	Silicon	EBL	T	30%	[182]

EBL: electron beam lithography; FIB: focused ion beam; T: transmission; R: reflection.

Despite the great advances in the development of metasurfaces, most existing devices are static in nature. Their functionalities cannot be tuned after fabrication [204]. Nowadays, various modulation mechanisms have been proposed to achieve dynamically tunable metasurfaces, such as electrical gating [36,205–209], optical control [210–214], thermal control [215–217], and mechanical actuation [218–220]. In these modulation mechanisms, apart from the traditional semiconductor materials, numerous functional materials such as graphene [205,221], phase-change materials [94,213,222–225], and liquid crystals [226–229], have been employed. This has prompted a large number of reconfigurable meta-devices at different wavelength bands (such as visible, IR, THz, microwave and millimeter wave regions). For reconfigurable metasurfaces in the IR band, the germanium-antimony-tellurium (GST) seems to be a good candidate owing to its large refractive index range across its phase transition from amorphous to crystalline [94]. Based on this property, several reconfigurable meta-devices have been achieved from the near-IR to the mid-IR [230–233]. However, achieving individual modulation of each pixel for real-time arbitrary wavefront steering remains a considerable challenge.

For most meta-devices in this review, large sets of meta-atom parameters are swept to create libraries, and proper meta-atoms are selected and assembled together to achieve meta-devices with desired optical responses. Recently, another design approach called inverse design, in which the desired optical response is defined as an objective cost function, has been proposed [234–237]. Several inverse design approaches such as the genetic algorithm [238], gradient-based algorithm [239], and deep learning algorithm [235,240,241] have been demonstrated. It is believed that the emerging inverse design approach will benefit the generation of broadband, high efficient and versatile polarization nanodevices.

Declaration of Competing Interest

The authors declare that they have no known competing financial interests or personal relationships that could have appeared to influence the work reported in this paper.

Acknowledgements

Guangtao Cao and He-Xiu Xu contributed equally to this work. The authors are grateful to Dr. Guangwei Hu for fruitful discussion and assistance. This work was supported by the National Research Foundation, Prime Minister's Office, Singapore, under its Competitive Research Program (CRP award number NRFCRP 22-2019-0006), the grant (R-261-518-004-720) from Advanced Research and Technology Innovation Centre (ARTIC), the National Natural Science Foundation of China (grant nos. 61974144, 61865006, 11564014 and 12004258), Guangdong Province Key Research and Development Plan (grant no. 2020B010174003), National Taipei University of Technology-Shenzhen University Joint Research Program (grant no. 2021009), the Science and Technology Foundation of Shenzhen (grant no. JSGG20191129114216474), the Natural Science Foundation of Hunan Province (grant no. 2019JJ50481), and the Education Department of Hunan Province (grant no. 18B324).

References

[1] N. Yu et al., Science 334 (2011) 333–337, https://doi.org/10.1126/science.1210713.
[2] S. Sun et al., Nat. Mater. 11 (2012) 426–431, https://doi.org/10.1038/nmat3292.
[3] A.M. Shaltout et al., Science 364 (2019) 6441, 10.1126science.aat3100.
[4] N. Yu, F. Capasso, Nat. Mater. 13 (2014) 139–150, https://doi.org/10.1038/nmat3839.
[5] Z. Dai et al., Chem. Rev. 120 (2020) 6197, https://doi.org/10.1021/acs.chemrev.9b00592.
[6] X. Yin et al., Science 339 (2013) 1405–1407, https://doi.org/10.1126/science.1231758.
[7] Y. Liu et al., Nanophotonics 6 (2017) 51–70, https://doi.org/10.1515/nanoph-2015-0155.
[8] Z. Cao et al., J. Phys. D: Appl. Phys. 52 (2019), https://doi.org/10.1088/1361-6463/ab36e9 435104.
[9] B. Wang et al., Nat. Nanotech. 15 (2020) 450–456, https://doi.org/10.1038/s41565-020-0670-0.
[10] J. Zhou et al., ACS Nano 12 (2018) 82–88, https://doi.org/10.1021/acsnano.7b07379.
[11] R. Jin et al., ACS Photonics 7 (2020) 512–518, https://doi.org/10.1021/acsphotonics.9b01608.
[12] M. Khorasaninejad et al., Science 352 (2016) 1190–1194, https://doi.org/10.1126/science.aaf6644.
[13] W. Liu et al., Adv. Mater. 30 (2018) 1706368, https://doi.org/10.1002/adma.201706368.
[14] S. Wang et al., Nat. Nanotech. 13 (2018) 227–232, https://doi.org/10.1038/s41565-017-0052-4.
[15] H. Yang et al., Opt. Mater. Express 8 (2018) 1940–1950, https://doi.org/10.1364/OME.8.001940.
[16] Q. Cheng et al., Sci. Bull. 64 (2019) 1525–1531, https://doi.org/10.1016/j.scib.2019.08.004.
[17] Z. Wang et al., Nat. Commun. 10 (2019) 3547, https://doi.org/10.1038/s41467-019-11578-y.
[18] H. Yang et al., Adv. Theory Simul. 2 (2019) 1800167, https://doi.org/10.1002/adts.201800167.
[19] H.-X. Xu et al., Appl. Phys. Lett. 109 (2016), https://doi.org/10.1063/1.4967438 193506.
[20] N. Yu et al., Nano Lett. 12 (2012) 6328–6333, https://doi.org/10.1021/nl303445u.
[21] S. Kruk et al., APL Photonics. 1 (2016), https://doi.org/10.1063/1.4949007 030801.
[22] W. Zang et al., Adv. Opt. Mater. 7 (2019) 1801747, https://doi.org/10.1002/adom.201801747.
[23] J. Li et al., Adv. Theory Simul. 3 (2020) 1900183, https://doi.org/10.1002/adts.201900183.
[24] L. Kang et al., Nano Lett. 20 (2020) 2047–2055, https://doi.org/10.1021/acs.nanolett.0c00007.
[25] Y. Nakata et al., Phys. Rev. Appl. 11 (2019), https://doi.org/10.1103/PhysRevApplied.11.044008 044008.
[26] Z. Li et al., Adv. Theory Simul. 2 (2019) 1900086, https://doi.org/10.1002/adts.201900086.
[27] H.-X. Xu et al., Sci. Rep. 6 (2016) 27503, https://doi.org/10.1038/srep27503.
[28] Kang et al., Nano Lett. 17 (2017) 7102–7109, https://doi.org/10.1021/acs.nanolett.7b03882.
[29] M. Kim et al., Adv. Opt. Mater. 5 (2017) 1700600, https://doi.org/10.1002/adom.201700600.
[30] S.-C. Jiang et al., Phys. Rev. X. 4 (2014), https://doi.org/10.1103/PhysRevX.4.021026 021026.
[31] Y.-J. Gao et al., Phys. Rev. X. 10 (2020), https://doi.org/10.1103/PhysRevX.10.031035 031035.
[32] Q. Song et al, Sci. Adv. 7 (2021) eabe1112, 10.1126/sciadv.abe1112.
[33] X. Ni, A.V. Kildishev, V.M. Shalaev, Nat. Commun. 4 (2013) 2807, https://doi.org/10.1038/ncomms3807.
[34] D. Wen et al., Nat. Commun. 6 (2015) 8241, https://doi.org/10.1038/ncomms9241.
[35] S.M. Kamali et al., Phys. Rev. X. 7 (2017), https://doi.org/10.1103/PhysRevX.7.041056 041056.
[36] L. Li et al., Nat. Commun. 8 (2017) 197, https://doi.org/10.1038/s41467-017-00164-9.

[37] J. Li et al., Sci. Adv. 4 (2018) aar6768, 10.1126/sciadv.aar6768.
[38] X. Fang, H. Ren, M. Gu, Nat. Photonics 14 (2020) 102–108, https://doi.org/10.1038/s41566-019-0560-x.
[39] Z. Wang et al., Opt. Lett. 45 (2020) 5488–5491, https://doi.org/10.1364/OL.403060.
[40] H. Zhou et al., ACS Nano 14 (2020) 5553–5559, https://doi.org/10.1021/acsnano.9b09814.
[41] C. Zhang et al., Light Sci. Appl. 9 (2020) 55, https://doi.org/10.1038/s41377-020-0287-y.
[42] X. Ding et al., PhotoniX 1 (2020) 16, https://doi.org/10.1186/s43074-020-00016-8.
[43] F. Yue et al., Adv. Mater. 29 (2017) 1603838, https://doi.org/10.1002/adma.201603838.
[44] H. Sroor et al., Nat. Photonics 14 (2020) 498–503, https://doi.org/10.1038/s41566-020-0623-z.
[45] Y. Shen et al., Light Sci. Appl. 8 (2019) 90, https://doi.org/10.1038/s41377-019-0194-2.
[46] Y. Liu et al., Sci. Rep. 7 (2017) 4096, https://doi.org/10.1038/srep44096.
[47] Y. Bao et al., Adv Mater. 32 (2020), https://doi.org/10.1002/adma.201905659 e1905659.
[48] Z.H. Jiang et al., Adv. Mater. 32 (2020), https://doi.org/10.1002/adma.201903983 e1903983.
[49] A.A. High et al., Nature 522 (2015) 192–196, https://doi.org/10.1038/nature14477.
[50] J. Lin et al., Science 340 (2013) 331–334, https://doi.org/10.1126/science.1233746.
[51] G. Cao et al., Opt. Express 21 (2013) 9198–9205, https://doi.org/10.1364/OE.21.009198.
[52] G. Cao et al., Opt. Lett. 39 (2014) 216–219, https://doi.org/10.1364/OL.39.000216.
[53] P. Li et al., Science 359 (2018) 892–896, https://doi.org/10.1126/science.aaq1704.
[54] W.Y. Tsai et al., Adv. Opt. Mater. 7 (2019) 1801060, https://doi.org/10.1002/adom.201801060.
[55] G. Cao et al., Opt. Express 22 (2014) 25215–25223, https://doi.org/10.1364/OE.22.025215.
[56] G. Hu et al., Nano Lett. 20 (2020) 3217–3224, https://doi.org/10.1021/acs.nanolett.9b05319.
[57] P. Li et al., Nat. Commun. 11 (2020) 3663, https://doi.org/10.1038/s41467-020-17425-9.
[58] G. Cao et al., Adv. Opt. Mater. 8 (2020) 1902153, https://doi.org/10.1002/adom.201902153.
[59] Y. Yang et al., Nano Lett. 20 (2020) 6774–6779, https://doi.org/10.1021/acs.nanolett.0c02699.
[60] G. Lin et al., Opt. Express 27 (2019) 33359–33368, https://doi.org/10.1364/OE.27.033359.
[61] L. Li, K. Yao, Z. Wang, Y. Liu, Laser Photonics Rev. 14 (2020) 1900244, https://doi.org/10.1002/lpor.201900244.
[62] L. Zhang et al., Nat. Commun. 9 (2018) 1481, https://doi.org/10.1038/s41467-018-03831-7.
[63] D.F. Barbin et al., Food Res. Int. 61 (2014) 23–32, https://doi.org/10.1016/j.foodres.2014.01.005.
[64] W. Liu et al., Iscience. 23 (2020), https://doi.org/10.1016/j.isci.2020.101868 101868.
[65] F. Ding et al., Adv. Opt. Mater. 7 (2019) 1801709, https://doi.org/10.1002/adom.201801709.
[66] G.-Y. Lee et al., Nanoscale. 10 (2018) 4237–4245, https://doi.org/10.1039/c7nr07154j.
[67] A.C. Overvig et al., Light Sci. Appl. 8 (2019) 92, https://doi.org/10.1038/s41377-019-0201-7.
[68] H.-X. Xu et al., Adv. Opt. Mater. 7 (2019) 1801479, https://doi.org/10.1002/adom.201801479.
[69] W. Ye et al., Nat. Commun. 7 (2016) 11930, https://doi.org/10.1038/ncomms11930.
[70] E. Minerbi, S. Keren-Zur, T. Ellenbogen, Nano Lett. 19 (2019) 6072–6077, https://doi.org/10.1021/acs.nanolett.9b01970.
[71] B. Sain, C. Meier, T. Zentgraf, Adv. Photonics 1 (2019), https://doi.org/10.1117/1.AP.1.2.024002 024002.
[72] H.-X. Xu et al., Adv. Mater. Tech. 5 (2020) 1900710, https://doi.org/10.1002/admt.201900710.
[73] H.-X. Xu et al., Adv. Opt. Mater. 6 (2018) 1800010, https://doi.org/10.1002/adom.201800010.
[74] W. Zang et al., Adv. Mater. 32 (2019) 1904935, https://doi.org/10.1002/adma.201904935.
[75] H.-X. Xu et al., Light: Sci. Appl. 10 (2021) 75, https://doi.org/10.1038/s41377-021-00507-8.
[76] A. Arbabi et al., Nat. Nanotechnol. 10 (2015) 937–943, https://doi.org/10.1038/nnano.2015.186.
[77] H.-X. Xu et al., Light Sci. Appl. 8 (2019) 3, https://doi.org/10.1038/s41377-018-0113-y.
[78] G. Hu et al., Trends. Chem. 3 (2021) 342–358, https://doi.org/10.1016/j.trechm.2021.02.004.
[79] R.C. Jones, Appl. Optics 31 (1941) 488–493, https://doi.org/10.1364/JOSA.31.000488.
[80] H.G. Berry, G. Gabrielse, A. Livingston, Appl. Optics 16 (1977) 3200–3205, https://doi.org/10.1364/AO.16.003200.
[81] R. Azzam, N. Bashara, Phys. Today 31 (1978) 72, https://doi.org/10.1063/1.2179193.
[82] D.G. Grier, Nature 424 (2003) 810–816, https://doi.org/10.1038/nature01935.
[83] B.K. Singh et al., Light Sci. Appl. 6 (2017), https://doi.org/10.1038/lsa.2017.50 e17050.
[84] X. Xie et al., Phys. Rev. Lett. 113 (2014), https://doi.org/10.1103/PhysRevLett.113.263901 263901.
[85] M. Mirhosseini et al., New J Phys. 17 (2015), https://doi.org/10.1088/1367-2630/17/3/033033 033033.
[86] N. Bozinovic et al., Science 340 (2013) 1545–1548, https://doi.org/10.1126/science.1237861.
[87] J. Fang et al., ACS Photonics 5 (2018) 3478–3484, https://doi.org/10.1021/acsphotonics.8b00680.
[88] G. Milione et al., Phys. Rev. Lett. 107 (2011), https://doi.org/10.1103/PhysRevLett.107.053601 053601.
[89] G. Milione et al., Phys. Rev. Lett. 108 (2012), https://doi.org/10.1103/PhysRevLett.108.190401 190401.
[90] H. Yang et al., Photon. Res. 9 (2021) 331–343, https://doi.org/10.1364/PRJ.411503.
[91] D. Naidoo et al., Nat. Photonics 10 (2016) 327–332, https://doi.org/10.1038/nphoton.2016.37.
[92] E.D. Palik, Handbook of Optical Constants of Solids, Academic press 3 (1998).
[93] T. Hu et al., Photonics Res. 5 (2017) 417–430, https://doi.org/10.1364/PRJ.5.000417.
[94] Y. Zhang et al., Nat. Commun. 10 (2019) 4279, https://doi.org/10.1038/s41467-019-12196-4.
[95] F. Ding et al., ACS Nano 9 (2015) 4111–4119, https://doi.org/10.1021/acsnano.5b00218.
[96] Y. Zhao, A. Alu, Nano Lett. 13 (2013) 1086–1091, https://doi.org/10.1021/nl304392b.
[97] Z. Ma et al., Opt. Lett. 43 (2018) 911–914, https://doi.org/10.1364/OL.43.000911.
[98] S. Gao et al., Nanoscale 11 (2019) 4083–4090, https://doi.org/10.1039/c9nr00187e.
[99] P.C. Wu et al., Nano Lett. 17 (2017) 445–452, https://doi.org/10.1021/acs.nanolett.6b04446.
[100] Y. Yang et al., Nano Lett. 14 (2014) 1394–1399, https://doi.org/10.1021/nl4044482.
[101] M. Wang et al., Nat. Commun. 11 (2020) 5055, https://doi.org/10.1038/s41467-020-18793-y.
[102] Z. Shi et al., Sci. Adv. 6 (2020) eaba3367, 10.1126/sciadv.aba3367.
[103] A. Shaltout et al., Nano Lett. 14 (2014) 4426–4431, https://doi.org/10.1021/nl501396d.
[104] P. Yu et al., Light Sci. Appl. 5 (2016) 16096, https://doi.org/10.1038/lsa.2016.96.
[105] H. Yang et al., Opt. Express 15 (2017) 16907–16915, https://doi.org/10.1364/OE.25.016907.
[106] T. Li et al., Opt. Express 25 (2017) 4216–4226, https://doi.org/10.1364/OE.25.004216.
[107] R. Zhao, L. Huang, Y. Wang, PhotoniX 1 (2020) 20, https://doi.org/10.1186/s43074-020-00020-y.
[108] Z.-L. Deng et al., Nano Lett. 18 (2018) 2885–2892, https://doi.org/10.1021/acs.nanolett.8b00047.
[109] R. Zhao et al., Light: Sci. Appl. 7 (2018) 95, https://doi.org/10.1038/s41377-018-0091-0.
[110] E. Arbabi, S.M. Kamali, A. Arbabi, A. Faraon, ACS Photonics 6 (2019) 2712–2718, https://doi.org/10.1021/acsphotonics.9b00678.

[111] R. Zhao et al., Adv. Funct. Mater. 31 (2021) 2100406, https://doi.org/10.1002/adfm.202100406.
[112] L. Yan et al., Int. J. Remote Sens. 41 (2020) 4853–4864, https://doi.org/10.1080/01431161.2020.1724350.
[113] A. Meindl, S. Loehle, S. Fasoulas, J. Appl. Phys. 128 (2020), https://doi.org/10.1063/5.0033375 233304.
[114] N.A. Rubin et al., Science 365 (2019) eaax1839, https://doi.org/10.1126/science.aax1839.
[115] G. Villarini W. F. Krajewski, Surv. Geophys. 31 (2010) 107-129, 10.1007/s10712-009-9079-x.
[116] J.B. Mueller et al., Phys. Rev. Lett. 118 (2017), https://doi.org/10.1103/physrevlett.118.113901 113901.
[117] Q. Fan, W. Zhu, et al., Nano Lett. 19 (2018) 1158–1165, https://doi.org/10.1021/acs.nanolett.8b04571.
[118] H.X. Xu et al., Annalen der physik. 529 (2017) 1700045, https://doi.org/10.1002/andp.201700045.
[119] Y. Hu et al., Nanophotonics 9 (2020) 3755–3780, https://doi.org/10.1515/nanoph-2020-0220.
[120] E. Arbabi et al., Acs Photonics 5 (2018) 3132–3140, https://doi.org/10.1021/acsphotonics.8b00362.
[121] L. Tong et al., Nat. Commun. 11 (2020) 2308, https://doi.org/10.1038/s41467-020-16125-8.
[122] S. Li et al., Adv. Opt. Mater. 7 (2018) 1801365, https://doi.org/10.1002/adom.201801365.
[123] C. Yan et al., Appl. Phys. Lett. 114 (2019), https://doi.org/10.1063/1.5091475 161904.
[124] K. Ou et al., Sci. Adv. 6 (2020) eabc0711, 10.1126/sciadv.abc0711.
[125] Z. Guo et al., J. Phys. D: Appl. Phys. 50 (2017), https://doi.org/10.1088/1361-6463/aa6f9b 254001.
[126] K. Chen et al., Adv. Mater. 32 (2020) 1906352, https://doi.org/10.1002/adma.201906352.
[127] M. Khorasaninejad et al., Sci. Adv. 2 (2016), https://doi.org/10.1126/sciadv.1501258 e1501258.
[128] B. Shen et al., Nat. Photonics 9 (2015) 378–382, https://doi.org/10.1038/nphoton.2015.80.
[129] N. Zhou et al., Sci. Adv. 5 (2019) 9593, https://doi.org/10.1126/sciadv.aau9593.
[130] L. Zhang et al., Adv. Funct. Mater. 28 (2018) 1802205, https://doi.org/10.1002/adfm.201802205.
[131] H. Yang et al., J. Phys. D: Appl. Phys. 54 (2020), https://doi.org/10.1088/1361-6463/abb7b8 015102.
[132] J. Wang, Chin. Opt. Lett. 16 (2018), https://doi.org/10.3788/col201816.050006 050006.
[133] M.W. Beijersbergen et al., Opt. Commun. 96 (1993) 123–132, https://doi.org/10.1016/0030-4018(93)90535-D.
[134] M. Beijersbergen et al., Opt. Commun. 112 (1994) 321–327, https://doi.org/10.1016/0030-4018(94)90638-6.
[135] L. Marrucci et al., J. Opt. 13 (2011), https://doi.org/10.1088/2040-8978/13/6/064001 064001.
[136] A. Forbes, A. Dudley, M. McLaren, Adv. Opt. Photonics 8 (2016) 200, https://doi.org/10.1364/aop.8.000200.
[137] X. Cai et al., Science 338 (2012) 363–366, https://doi.org/10.1126/science.1226528.
[138] E. Karimi et al., Light Sci. Appl. 3 (2014), https://doi.org/10.1038/lsa.2014.48 e167.
[139] Y. Liu et al., Appl. Phys. Lett. 104 (2014), https://doi.org/10.1063/1.4878409 191110.
[140] K.E. Chong et al., Nano Lett. 15 (2015) 5369–5374, https://doi.org/10.1021/acs.nanolett.5b01752.
[141] E. Maguid et al., Science 352 (2016) 1202–1206, https://doi.org/10.1126/science.aaf3417.
[142] J. Zeng et al., Nano Lett. 16 (2016) 3101–3108, https://doi.org/10.1021/acs.nanolett.6b00360.
[143] L. Huang et al., ACS Photonics 4 (2017) 338–346, https://doi.org/10.1021/acsphotonics.6b00808.
[144] K. Ou et al., Nanoscale 10 (2018) 19154–19161, https://doi.org/10.1039/c8nr07480a.
[145] R. Wang et al., Opt. Lett. 43 (2018) 3570–3573, https://doi.org/10.1364/OL.43.003570.
[146] X. Wang et al., Nanophotonics 7 (2018) 1533–1556, https://doi.org/10.1515/nanoph-2018-0072.
[147] Z. Xie et al., Light Sci. Appl. 7 (2018) 18001, https://doi.org/10.1038/lsa.2018.1.
[148] H. Yang et al., J. Phys. D: Appl. Phys. 53 (2019), https://doi.org/10.1088/1361-6463/ab51fd 045104.
[149] R.C. Devlin et al., Science 358 (2017) 896–901, https://doi.org/10.1126/science.aao5392.
[150] R.C. Devlin et al., Opt. Express 25 (2017) 377–393, https://doi.org/10.1364/OE.25.000377.
[151] Y. Zhang et al., Adv. Opt. Mater. 6 (2018) 1701228, https://doi.org/10.1002/adom.201701228.
[152] Z. Li et al., Adv. Opt. Mater. 4 (2016) 1230–1235, https://doi.org/10.1002/adom.201600108.
[153] W.T. Chen et al., Light: Sci. Appl. 6 (2017) e16259-e16259, 10.1038/lsa.2016.259.
[154] T. Wang et al., Adv. Theory Simul. 2 (2019) 1900071, https://doi.org/10.1002/adts.201900071.
[155] Y. Guo et al., Adv. Opt. Mater. 7 (2019) 1900503, 10.1002/adom.201900503.
[156] T. Li et al., Phys. Rev. Appl. 15 (2021), https://doi.org/10.1103/PhysRevApplied.15.014059 014059.
[157] M. Padgett, R.J. Bowman, Nat. Photonics 5 (2011) 343–348, https://doi.org/10.1038/nphoton.2011.81.
[158] C. Min et al., Nat. Commun. 4 (2013) 2891, https://doi.org/10.1038/ncomms3891.
[159] Y. Ma et al., Sci. Rep. 7 (2017) 14611, https://doi.org/10.1038/s41598-017-14449-y.
[160] M. He et al., IEEE Access 8 (2020) 37275–37280, https://doi.org/10.1109/ACCESS.2020.2975291.
[161] T. Chantakit et al., Photon. Res. 8 (2020) 1435–1440, https://doi.org/10.1364/PRJ.389200.
[162] M. Xian et al., Sci. Bull. 65 (2020) 2072, https://doi.org/10.1016/j.scib.2020.07.016.
[163] T. Zhu et al., Nat. Commun. 8 (2017) 15391, https://doi.org/10.1038/ncomms15391.
[164] T. Zhu et al., Phys. Rev. Appl. 11 (2019), https://doi.org/10.1103/PhysRevApplied.11.034043 034043.
[165] Y. Zhou et al., Nat. Photonics 14 (2020) 316–323, https://doi.org/10.1038/s41566-020-0591-3.
[166] P. Huo et al., Nano Lett. 20 (2020) 2791–2798, https://doi.org/10.1021/acs.nanolett.0c00471.
[167] S. Li et al., Adv. Opt. Mater. 8 (2020) 1901666, https://doi.org/10.1002/adom.201901666.
[168] H. Zhao et al., ACS Photonics 5 (2017) 1726–1732, https://doi.org/10.1021/acsphotonics.7b01149.
[169] L. Gong et al., Light Sci. Appl. 8 (2019) 27, https://doi.org/10.1038/s41377-019-0140-3.
[170] Y. Li et al., Adv. Opt. Mater. 5 (2017) 1600502, https://doi.org/10.1002/adom.201600502.
[171] H. Ren et al., Nat. Commun. 10 (2019) 2986, https://doi.org/10.1038/s41467-019-11030-1.
[172] H. Ren et al., Nat. Nanotechnol. 15 (2020) 948, https://doi.org/10.1038/s41565-020-0768-4.
[173] R. Xu et al., Phys. Rev. Appl. 10 (2018), https://doi.org/10.1103/PhysRevApplied.10.034061 034061.
[174] F. Afshinmanesh et al., Nanophotonics 1 (2012) 125–129, https://doi.org/10.1515/nanoph-2012-0004.
[175] L. Du et al., Nat. Commun. 6 (2015) 10051, https://doi.org/10.1038/ncomms.10051.
[176] A. Pors, M.G. Nielsen, S.I. Bozhevolnyi, Optica 2 (2015) 716, https://doi.org/10.1364/optica.2.000716.
[177] J.P. Balthasar Mueller, K. Leosson, F. Capasso, Optica 3 (2016) 42, 10.1364/optica.3.000042.
[178] H. Yang et al., Opt. Express 26 (2018) 5632–5643, https://doi.org/10.1364/OE.26.005632.
[179] N.A. Rubin et al., Science 365 (2019) 6448, https://doi.org/10.1126/science.aax1839.
[180] X. Zhang et al., Optica 6 (2019) 190, https://doi.org/10.1364/optica.6.001190.
[181] J. Wei et al., Nat. Commun. 11 (2020) 6404, https://doi.org/10.1038/s41467-020-20115-1.
[182] Y. Wang et al., Photon. Res. 8 (2020) 482, https://doi.org/10.1364/prj.383772.
[183] A. Ma et al., Adv. Opt. Mater. 8 (2020) 2000484, https://doi.org/10.1002/adom.202000484.
[184] F. Yue et al., Adv. Mater. Tech. 5 (2020) 1901008, https://doi.org/10.1002/admt.201901008.

[185] W. Li et al., Nat. Commun. 6 (2015) 8379, https://doi.org/10.1038/ncomms9379.
[186] Z. Wang et al., Acs Photonics 3 (2016) 2096–2101, https://doi.org/10.1021/acsphotonics.6b00533.
[187] J. Bai et al., Photonics Res. 7 (2019) 1051–1060, https://doi.org/10.1364/PRJ.7.001051.
[188] Z. Yang et al., Nat. Commun. 9 (2018) 4607, https://doi.org/10.1038/s41467-018-07056-6.
[189] S. Wei, Z. Yang, M. Zhao, Opt. Lett. 42 (2017) 1580–1583, https://doi.org/10.1364/OL.42.001580.
[190] S. Mei et al., Nanoscale 8 (2016) 2227–2233, https://doi.org/10.1039/c5nr07374j.
[191] J. Chen et al., Laser Photonics Rev. 12 (2018) 1700331.
[192] H. Yang et al., Adv. Theory Simul. 2 (2019) 1900133, https://doi.org/10.1002/adts.201900133.
[193] X. Zhao et al., ACS Photonics 7 (2019) 212–220, https://doi.org/10.1021/acsphotonics.9b01437.
[194] F. Feng et al., Light Sci. Appl. 9 (2020) 95, https://doi.org/10.1038/s41377-020-0330-z.
[195] Y. Fu et al., Nanoscale 11 (2019) 18303–18310, https://doi.org/10.1039/c9nr05811g.
[196] S. Zhang et al., Laser Photonics Rev. 14 (2020) 2000062, https://doi.org/10.1002/lpor.202000062.
[197] Y. Guo et al., Light: Sci. Appl. 10 (2021) 63, https://doi.org/10.1038/s41377-021-00497-7.
[198] G. Ding et al., Phys. Rev. Appl. 11 (2019), https://doi.org/10.1103/PhysRevApplied11.044043 044043.
[199] G. Hu et al., Nat. Photonics 13 (2019) 467, https://doi.org/10.1038/s41566-019-0399-1.
[200] G. Hu et al., Nature 582 (2020) 209–213, https://doi.org/10.1038/s41586-020-2359-9.
[201] G. Li et al., Nat. Rev. Mater. 2 (2017) 17010, https://doi.org/10.1038/natrevmats.2017.10.
[202] X. Hong et al., Research 2020 (2020) 9085782, 10.34133/2020/9085782.
[203] R. Zhou et al., Nanoscale 10 (2018) 18878–18891, https://doi.org/10.1039/C8NR06796A.
[204] Y.-W. Huang et al., Proc. IEEE 108 (2019) 772–794, https://doi.org/10.1109/JPROC.2019.2919675.
[205] Z. Fei et al., Nature 487 (2012) 82–85, https://doi.org/10.1038/nature11253.
[206] J. Li et al., Adv. Opt. Mater. 4 (2016) 91–98, https://doi.org/10.1002/adom.201500398.
[207] C. Huang et al., ACS Photonics 5 (2017) 1718–1725, https://doi.org/10.1021/acsphotonics.7b01114.
[208] J. Park et al., Nano Lett. 17 (2017) 407–413, https://doi.org/10.1021/acs.nanolett.6b04378.
[209] X.-J. Shang et al., New J. Phys. 22 (2020), https://doi.org/10.1088/1367-2630/ab9428 063054.
[210] M.Z. Alam, I. De Leon, R.W. Boyd, Science 352 (2016) 795–797, https://doi.org/10.1126/science.aae0330.
[211] M.Z. Alam et al., Nat. Photonics 12 (2018) 79–83, https://doi.org/10.1038/s41566-017-0089-9.
[212] X.G. Zhang et al., Nat. Electron. 3 (2020) 165–171, https://doi.org/10.1038/s41928-020-0380-5.
[213] A. Leitis et al., Adv. Funct. Mater. 30 (2020) 1910259, https://doi.org/10.1002/adfm.201910259.
[214] J. Li et al., Nano Lett. 21 (2021) 973–979, https://doi.org/10.1021/acs.nanolett.0c03957.
[215] J. Sautter et al., ACS Nano 9 (2015) 4308–4315, https://doi.org/10.1021/acsnano.5b00723.
[216] A. Komar et al., ACS Photonics 5 (2018) 1742-1742, 10.1021/acsphotonics.7b01343.
[217] T. Wei et al., Adv. Opt. Mater. 8 (2020) 1902033, https://doi.org/10.1002/adom.201902033.
[218] S.M. Kamali et al., Laser Photonics Rev. 10 (2016) 1002–1008, https://doi.org/10.1002/lpor.201600144.
[219] A.L. Holsteen et al., Science 358 (2017) 1407–1410, https://doi.org/10.1126/science.aao5371.
[220] E. Arbabi et al., Nat. Commun. 9 (2018) 812, https://doi.org/10.1038/s41467-018-03155-6.
[221] Z. Liu et al., New J. Phys. 22 (2019), https://doi.org/10.1088/1367-2630/ab83d5 053039.
[222] Q. Wang et al., Nat. Photonics 10 (2015) 60–65, https://doi.org/10.1038/nphoton.2015.247.
[223] F.Z. Shu et al., Adv. Opt. Mater. 6 (2018) 1700939, https://doi.org/10.1002/adom.201700939.
[224] Y. Zhang et al., Nat. Nanotechnol. (2021) 1–6, https://doi.org/10.1038/s41565-021-00881-9.
[225] M.Y. Shalaginov et al., Nat. Commun. 12 (2021) 1225, https://doi.org/10.1038/s41467-021-21440-9.
[226] P. Chen et al., Adv. Mater. 32 (2020) 1903665, https://doi.org/10.1002/adma.201903665.
[227] R.S. Zola et al., Adv. Mater. 31 (2019) 1806172, https://doi.org/10.1002/adma.201806172.
[228] S.-Q. Li et al., Science 364 (2019) 1087-1090, 10.1126science.aaw6747.
[229] I. Kim et al., Adv. Mater. 32 (2020) 2004664, https://doi.org/10.1002/adma.202004664.
[230] C.H. Chu et al., Laser Photonics Rev. 10 (2016) 986–994, https://doi.org/10.1002/lpor.201600106.
[231] C.R. de Galarreta et al., Adva. Funct. Mater. 28 (2018) 1704993, https://doi.org/10.1002/adfm.201704993.
[232] F. Zhang et al., Adv. Mater. 32 (2020) 1908194, https://doi.org/10.1002/adma.201908194.
[233] M.N. Julian et al., Optica 7 (2020) 746–754, https://doi.org/10.1364/OPTICA.392878.
[234] S. Molesky et al., Nat. Photonics 12 (2018) 659–670, https://doi.org/10.1038/s41566-018-0246-9.
[235] Z. Liu et al., Nano Lett. 18 (2018) 6570–6576, https://doi.org/10.1021/acs.nanolett.8b03171.
[236] W. Ma, F. Cheng, Y. Liu, ACS Nano 12 (2018) 6326–6334, https://doi.org/10.1021/acsnano.8b03569.
[237] W. Ma et al., Adv. Mater. 31 (2019) 1901111, https://doi.org/10.1002/adma.201901111.
[238] Z. Jin et al., ACS nano 13 (2019) 821–829, https://doi.org/10.1021/acsnano.8b08333.
[239] M.M. Elsawy et al., Laser Photonics Rev. 14 (2020) 1900445, https://doi.org/10.1002/lpor.201900445.
[240] W. Ma et al., Nat. Photonics 15 (2020) 77–90, https://doi.org/10.1038/s41566-020-0685-y.
[241] Z. Liu et al., Adv. Mater. 32 (2020) 1904790, https://doi.org/10.1002/adma.201904790.